

Improving Short-Term QPF Using Geostationary Satellite All-Sky Infrared Radiances: Real-Time Ensemble Data Assimilation and Forecast during the PRECIP 2020 and 2021 Experiments

YUNJI ZHANG^{a,b,c}, XINGCHAO CHEN^{a,c} AND MICHAEL M. BELL^d

^a Center for Advanced Data Assimilation and Predictability Techniques, The Pennsylvania State University, University Park, Pennsylvania

^b Alliance for Education, Science, Engineering, and Design with Africa, The Pennsylvania State University, University Park, Pennsylvania

^c Department of Meteorology and Atmospheric Science, The Pennsylvania State University, University Park, Pennsylvania

^d Department of Atmospheric Science, Colorado State University, Fort Collins, Colorado

(Manuscript received 30 August 2022, in final form 31 January 2023)

ABSTRACT: The Prediction of Rainfall Extremes Campaign In the Pacific (PRECIP) aims to improve our understanding of extreme rainfall processes in the East Asian summer monsoon. A convection-permitting ensemble-based data assimilation and forecast system (the PSU WRF-EnKF system) was run in real time in the summers of 2020–21 in advance of the 2022 field campaign, assimilating all-sky infrared (IR) radiances from the geostationary *Himawari-8* and *GOES-16* satellites, and providing 48-h ensemble forecasts every day for weather briefings and discussions. This is the first time that all-sky IR data assimilation has been performed in a real-time forecast system at a convection-permitting resolution for several seasons. Compared with retrospective forecasts that exclude all-sky IR radiances, rainfall predictions are statistically significantly improved out to at least 4–6 h for the real-time forecasts, which is comparable to the time scale of improvements gained from assimilating observations from the dense ground-based Doppler weather radars. The assimilation of all-sky IR radiances also reduced the forecast errors of large-scale environments and helped to maintain a more reasonable ensemble spread compared with the counterpart experiments that did not assimilate all-sky IR radiances. The results indicate strong potential for improving routine short-term quantitative precipitation forecasts using these high-spatiotemporal-resolution satellite observations in the future.

SIGNIFICANCE STATEMENT: During the summers of 2020/21, the PSU WRF-EnKF data assimilation and forecast system was run in real time in advance of the 2022 Prediction of Rainfall Extremes Campaign In the Pacific (PRECIP), assimilating all-sky (clear-sky and cloudy) infrared radiances from geostationary satellites into a numerical weather prediction model and providing ensemble forecasts. This study presents the first-of-its-kind systematic evaluation of the impacts of assimilating all-sky infrared radiances on short-term qualitative precipitation forecasts using multiyear, multiregion, real-time ensemble forecasts. Results suggest that rainfall forecasts are improved out to at least 4–6 h with the assimilation of all-sky infrared radiances, comparable to the influence of assimilating radar observations, with benefits in forecasting large-scale environments and representing atmospheric uncertainties as well.

KEYWORDS: Forecast verification/skill; Numerical weather prediction/forecasting; Short-range prediction; Data assimilation; Ensembles

1. Introduction

Extreme rainfall and its associated hazards, such as flash flooding and landslides, are impactful weather phenomena that threaten human lives and properties worldwide. Improving the short-term forecasts of extreme rainfall, i.e., quantitative precipitation forecasts (QPFs) at 0–12-h forecast lead time, is therefore crucial. However, our knowledge of the fundamental processes that lead to extreme rainfall is incomplete and our ability to forecast these events remains limited.

To improve our understanding of the dynamical, thermodynamical, and microphysical processes associated with extreme rainfall as well as their predictability, the Prediction of Rainfall

Extremes Campaign In the Pacific (PRECIP) was proposed to take place in Taiwan and Japan from late May to early August of 2020 as a collaborative effort across multiple universities and institutions internationally. The field phase of PRECIP was designed to observe extreme rainfall events ranging from local rainstorms, mei-yu fronts, to typhoons, in the moisture-rich environment of the East Asian monsoon region. Although the primary field phase of PRECIP was postponed to 2022 due to the COVID-19 pandemic, some activities were carried out during the same period of 2020 and 2021 summers in Taiwan and Japan as pilot studies; additionally, the Preparatory Rockies Experiment for the Campaign in the Pacific (“PRE”-CIP) was carried out from mid-July to mid-August of 2021 in Colorado, United States, during the North American monsoon season, providing datasets complementary to those gathered in Taiwan and Japan. Hereafter, we will refer to experiments in East Asia during the 2020 and 2021 summers as PRECIP2020 and PRECIP2021, and experiments in Colorado during the 2021 summer as “PRE”-CIP2021.

Supplemental information related to this paper is available at the Journals Online website: <https://doi.org/10.1175/WAF-D-22-0156.s1>.

Corresponding author: Yunji Zhang, yuz31@psu.edu

DOI: 10.1175/WAF-D-22-0156.1

© 2023 American Meteorological Society. For information regarding reuse of this content and general copyright information, consult the [AMS Copyright Policy \(www.ametsoc.org/PUBSReuseLicenses\)](https://www.ametsoc.org/PUBSReuseLicenses).

The holistic PRECIP field campaign was designed to have both observational and modeling components. The modeling component in the 2020 and 2021 summer seasons included 1) real-time convection-permitting deterministic forecasts using the Model for Prediction Across Scales (MPAS; Skamarock et al. 2012) with a global variable-resolution domain that uses a 3-km convection-permitting grid spacing in Taiwan and surrounding area and a 15-km grid spacing elsewhere; and 2) real-time convection-permitting ensemble forecasts using the Pennsylvania State University (PSU) Weather Research and Forecasting (WRF) ensemble Kalman filter (EnKF) regional data assimilation and forecast system (the PSU WRF-EnKF system; Zhang et al. 2009; Weng and Zhang 2012). The PSU WRF-EnKF system was run in real time for PRECIP2020, PRECIP2021, and “PRE”-CIP2021 in advance of the 2022 primary field campaign. This study focuses on the 2020 and 2021 forecasts which were conducted with limited field observations due to the COVID pandemic. The results from the 2022 observational field campaign and associated modeling components will be reported in a future study.

One of the highlights of the real-time PSU WRF-EnKF forecasts for PRECIP is the assimilation of satellite all-sky infrared (IR) brightness temperatures (BTs; used interchangeably with “radiance” hereafter) from the Advanced Himawari Imager (AHI) onboard the *Himawari-8* geostationary satellite of Japan and the Advanced Baseline Imager (ABI) onboard the *GOES-16* geostationary satellite of the United States. Improving QPF remains one of the biggest challenges of numerical weather predictions (NWP). Assimilations of Doppler weather radar observations have been shown to improve short-term QPF at 0–6-h forecast lead time (e.g., Xiao and Sun 2007; Aksoy et al. 2010; Clark et al. 2012; Johnson et al. 2015; Surcel et al. 2015; Yussouf et al. 2016; Schwartz et al. 2021). Compared with Doppler weather radars that are mostly located inland and can only observe the rainfall after precipitation hydrometeors are formed, infrared sensors onboard geostationary satellites can detect the formation of clouds before the formation of precipitation with relatively high spatiotemporal resolutions over both ocean and land.

Currently, only clear-sky IR BTs are assimilated in operational NWP models at coarse resolutions (>10 km; Geer et al. 2018) due to the complexities associated with all-sky (i.e., clear-sky and cloudy) IR BT assimilations (e.g., Geer and Bauer 2011). Geer et al. (2018) shows that the European Centre for Medium-Range Weather Forecasts (ECMWF), the Japan Meteorological Agency (JMA), the National Centers for Environmental Prediction (NCEP), the Met Office (United Kingdom), and Météo-France are assimilating clear-sky IR BTs from the geostationary satellites into their global models, and JMA and NCEP are developing the capability to assimilate all-sky IR BTs for their global models. Aside from all-sky IR BTs from geostationary satellites, operational NWP centers are also actively developing the capability of assimilating all-sky IR BTs from hyperspectral infrared sounders onboard low-Earth-orbiting (LEO) satellites, which have much more moisture-sensitive channels compared with the moisture-sensitive IR image channels of AHI and ABI, as well as all-sky microwave (MW) BTs from LEO satellites, which are

sensitive to different types of hydrometeors at different spectral bands. However, the temporal resolutions of the LEO satellites are relatively coarse, such that they are suitable for the 3–6-h assimilation time windows of the global models, but they are not able to capture the rapid development of the convective-to-mesoscale rainfall systems. On the other hand, ground-based Doppler weather radars have adequate spatiotemporal resolutions to resolve convection, but their limited spatial coverage prohibits their monitoring of rainfall systems far from land. Besides, the blocking effects of topography, trees, and buildings further limit ground-based radars’ ability to detect storms over some regions. IR BTs from geostationary satellites can provide continuous, seamless observations of rainfall systems with high spatiotemporal resolutions.

There have been significant enhancements in our ability to ingest all-sky IR BTs from geostationary satellites into convection-permitting regional models using ensemble-based data assimilation techniques (such as EnKF) in recent years. Numerous studies utilizing convection-permitting models have already shown that the assimilation of all-sky IR BTs can improve predictions of tropical cyclones (TCs; F. Zhang et al. 2016, 2019; Honda et al. 2018a; Minamide and Zhang 2018; Minamide et al. 2020; Hartman et al. 2021), severe thunderstorms (Y. Zhang et al. 2018, 2019; Jones et al. 2020), and other convective systems (Honda et al. 2018b; Otkin and Potthast 2019; Sawada et al. 2019; Chan et al. 2020b). However, their potential impacts on the short-term QPF (0–12-h) have not been systematically explored using long-term and real-time data assimilation experiments.

In this study, we show that all-sky IR BTs have the potential to improve rainfall predictions in different regions through advanced ensemble-based data assimilation techniques. To the best of our knowledge, the real-time operation of the PSU WRF-EnKF system during PRECIP is the first time that a regional, convection-permitting, ensemble-based data assimilation and forecast system running in real-time has assimilated all-sky IR BTs. This study does not aim at improving our capability to assimilate all-sky IR BTs, but rather presents a systematic evaluation of the potential of improving the short-term QPF in real-time at both convective gray-zone and convection-permitting resolutions. The rainfall associated with mei-yu/baiu fronts in China, Korea, and Japan in the warm season of 2020 is also above the climate average (e.g., Takaya et al. 2020), leading to devastating floods. This also provides a good opportunity to evaluate the impacts of all-sky IR data assimilation on the real-time forecasts of extreme rainfall.

2. Configurations of the real-time PSU WRF-EnKF system

a. Configurations for PRECIP2020

The PSU WRF-EnKF system configured for the PRECIP experiments combines the Advanced Research WRF (ARW/WRF; Skamarock et al. 2019) model, version 4.2, the ensemble square root filter (EnSRF; Houtekamer and Mitchell 2001) variation of EnKF, and the Community Radiative Transfer Model (CRTM; Han et al. 2006), version 2.3.0. For PRECIP2020, the

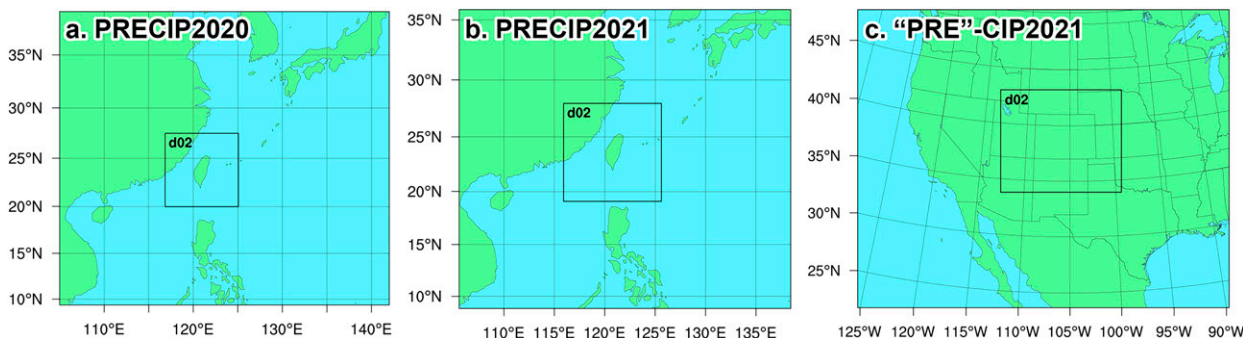


FIG. 1. PSU WRF-EnKF domain configurations for (a) PRECIP2020, (b) PRECIP2021, and (c) “PRE”-CIP2021 experiments.

system is configured with a $450 \times 400 \times 50$ domain with a horizontal grid spacing of 9 km, covering East Asia and part of the western North Pacific, and a one-way nested 3-km domain of $300 \times 300 \times 50$ grids covering Taiwan and adjacent regions (Fig. 1a). The hybrid sigma-pressure vertical coordinate is used to deal with the complex terrain over the Taiwan and Luzon islands and the Indochinese Peninsula, and the highest model level is located at 50 hPa. Employed physical parameterization schemes include the aerosol-aware version of the Thompson microphysics scheme (Thompson and Eidhammer 2014), the revised MM5 Monin–Obukhov scheme for surface layer processes (Jiménez et al. 2012), the Noah land surface model (Tewari et al. 2004), the YSU scheme for PBL processes (Hong et al. 2006), and the RRTMG scheme for longwave and shortwave radiations (Iacono et al. 2008). No cumulus scheme is applied in both domains.

The PSU WRF-EnKF system uses 40 ensemble members, which is a balance between available computational resources and the need to reduce sampling errors and underdispersive ensembles that result from limited ensemble members. Similar ensemble sizes of around 40 have been successfully used for other studies assimilating all-sky IR BTs using EnKF at convection-permitting resolutions (e.g., Otkin and Potthast 2019; Y. Zhang et al. 2018, 2019; Jones et al. 2020). The system also uses adaptive observation error inflation (AOEI; Minamide and Zhang 2017) and adaptive observation error background inflation (ABEI; Minamide and Zhang 2018) to treat the nonlinearities and non-Gaussianities associated with the IR BTs, which have been proven to improve the assimilation of all-sky IR BTs by numerous studies (e.g., F. Zhang et al. 2019; Minamide and Zhang 2017, 2018, 2019; Y. Zhang et al. 2018, 2019, 2021a; Minamide et al. 2020; Chan et al. 2020b; Minamide and Posselt 2021; Hartman et al. 2021). The relaxation-to-prior-perturbation (RTPP; Zhang et al. 2004) method is used to maintain ensemble spread and combines 80% of the prior perturbations and 20% of the posterior perturbations.

The system was run in real time from 20 May to 10 August 2020 once daily for PRECIP2020 (83 days in total). Initial conditions of the 40 ensemble members at 0000 UTC every day were generated using the 20-member Global Ensemble Forecasting System (GEFS) analyses at 0000 UTC of the same day, and 20-member 6-h GEFS forecasts from 1800 UTC of the

previous day valid also at 0000 UTC of the current day. Values at GEFS grids are horizontally and vertically interpolated to the WRF grids. After a spinup period of 3 h, hourly EnKF cycling data assimilations were performed till 1200 UTC (i.e., 10 data assimilation cycles in total). Assimilated observations including conventional surface, rawinsonde, and commercial aircraft observations from the Global Telecommunication System (GTS) acquired through the Meteorological Assimilation Data Ingest System (MADIS) and all-sky IR BTs from the $7.3\text{-}\mu\text{m}$ channel 10 (lower-tropospheric water vapor channel) of *Himawari-8*'s AHI. The raw IR BTs were thinned to a horizontal spacing of 0.2° (roughly 20 km) for the outer domain and 0.04° (roughly 4 km) for the inner domain, and they were assimilated with no vertical localization and horizontal radii of influence (ROI; in terms of cutoff distance where the observations' impacts reduce to zero) of 100 and 40 km for the outer and inner domains. No additional quality control or bias correction procedures were performed following previous practices (F. Zhang et al. 2019; Minamide and Zhang 2017, 2018, 2019; Y. Zhang et al. 2018, 2019, 2021a; Minamide et al. 2020; Chan et al. 2020b; Minamide and Posselt 2021; Hartman et al. 2021) due to the inability for a regional model to separate errors in model fields from systematic biases associated with the parameterization schemes and the radiative transfer model. After the final analysis at 1200 UTC of each day, a 40-member 48-h ensemble forecast was carried out.

The daily 48-h ensemble forecasts described above will be referred to as the “RT2020” (“real-time 2020”) forecasts hereafter. As a comparison, a parallel experiment following the same manner as RT2020 but excluding IR BTs during cycling EnKF was performed retrospectively after the field campaign, and its ensemble forecasts will be referred to as the “NoIR2020” forecasts hereafter. Our purpose is to create “twin” forecasts that only differ from the real-time forecasts by not assimilating all-sky IR BTs, therefore the system configurations are kept identical. Due to limited extreme rainfall events near Taiwan during the pilot study resulting from the unexpectedly calm western North Pacific in 2020, as well as limited computational resources, the retrospective NoIR2020 experiment only uses the 9-km outer domain for both the data assimilations and the ensemble forecasts, and the verification of the RT2020 and NoIR2020 forecasts will be focused on the 9-km domain as well. Although the 9-km grid spacing is unable to resolve isolated convective

TABLE 1. Differences in the configurations of the PSU WRF-EnKF system during the PRECIP2020, PRECIP2021, and “PRE”-CIP2021 experiments (see section 2b for details).

	PRECIP2020 (Taiwan)	PRECIP2021 (Taiwan)	“PRE”-CIP2021 (Colorado)
WRF configuration			
ARW-WRF version	4.2	4.3	4.3
9-km domain size	450 × 400 × 50	400 × 360 × 50	400 × 320 × 50
3-km domain size	300 × 300 × 50	354 × 354 × 50	390 × 330 × 50
Microphysics	Thompson aerosol	Thompson aerosol	Thompson
Surface	Monin–Obukhov	Monin–Obukhov	MYNN
Land surface model	Noah	Noah	RUC
PBL	YSU	YSU	MYNN 2.5
SKEB and SPPT	No	Yes	Yes
Forecast length	40-member 48-h	40-member 12-h and 20-member 48-h	40-member 12-h and 20-member 48-h
EnKF configuration			
Satellite and sensor	<i>Himawari-8</i> AHI	<i>Himawari-8</i> AHI	<i>GOES-16</i> ABI
9-km-domain BT ROI	100 km	40 km	40 km
Multiplicative inflation	No	1%	1%

cells, this model resolution can capture the primary characteristics of mesoscale systems that contribute most monsoonal precipitation, and it has been widely used in simulating tropical and monsoonal rainfall with adequate skill (e.g., Wang et al. 2015; Chen et al. 2018, 2021, 2022a; Chen and Zhang 2019; He et al. 2019; Ou et al. 2020; Ruppert and Chen 2020). Limited by computational resources, we also did not perform additional retrospective experiments to compare the impact of clear-sky versus all-sky IR BTs. Okamoto et al. (2019) showed that compared with when only clear-sky IR BTs are assimilated, the assimilation of all-sky IR BTs leads to reduced errors against independent conventional observations and satellite retrievals and improved rainfall forecasts.

b. Configurations for PRECIP2021 and “PRE”-CIP2021

Based on preliminary analyses performed after PRECIP2020, several adjustments were made to the PSU WRF-EnKF system for its PRECIP2021 and the “PRE”-CIP2021 (assimilating channel-10 IR BTs from *GOES-16*'s ABI, which has an identical 7.3- μm wavelength to channel 10 of *Himawari-8*'s AHI) real-time runs. Unless otherwise noted, all the changed configurations described below are applied to both the PRECIP2021 and the “PRE”-CIP2021 domains. The differences in the system configurations are also summarized in Table 1.

The latest version 4.3 of ARW/WRF was used instead of version 4.2. The domain configurations for PRECIP2021 were adjusted (Fig. 1b) with the area covered by the 3-km domain increased by 40% to 354 × 354 compared with the PRECIP2020 configuration of 300 × 300 and the area covered by the 9-km domain slightly decreased to 400 × 360 to compensate the increased 3-km computational costs. The 9-km domain (400 × 320 × 50) of “PRE”-CIP2021 covers the western 2/3 of the contiguous United States (CONUS) and the 3-km domain (390 × 330 × 50) covers Colorado and the surrounding area. While PRECIP2021 inherits the same set of physical parameterization schemes from PRECIP2020, the “PRE”-CIP2021 runs use a slightly different combination of parameterization schemes, including the Thompson et al. (2008) microphysics, the Mellor–Yamada–Nakanishi–Niino (MYNN)

surface scheme (Nakanishi and Niino 2004), the RUC land surface model (Benjamin et al. 2004), and the MYNN 2.5-level TKE scheme for PBL processes (Nakanishi and Niino 2004). These schemes are also used by the operational High-Resolution Rapid Refresh (HRRR) model and are expected to provide satisfactory performance for convection over CONUS at a 3-km horizontal grid spacing.

One outstanding issue associated with the PRECIP2020 forecasts is that the ensemble forecasts are generally underdispersive (see section 4 for more details), which is also an issue that has been frequently observed in regional ensemble prediction systems (e.g., Schumacher and Clark 2014; Schwartz et al. 2014; Hagelin et al. 2017). To combat the ensemble underdispersiveness, we applied stochastic kinetic energy backscatter (SKEB; Mason and Thompson 1992) and stochastically perturbed physics tendencies (SPPT; Buizza et al. 1999) schemes for the PRECIP2021 and “PRE”-CIP2021 runs with different random seeds assigned for each of the ensemble members, as well as multiplicative covariance inflation of prior perturbations for EnKF (Anderson and Anderson 1999) by increasing the magnitudes of EnKF prior perturbations by 1% before assimilating observations for all EnKF cycles. The impacts of applying these additional methods are examined in section 4. The horizontal ROI for the outer 9-km domain is also reduced from 100 to 40 km based on our recent study on the structure of correlations between all-sky IR BTs and atmospheric states (Zhang et al. 2021b, 2022a).

Additionally, preliminary quantitative verifications based on the PRECIP2020 forecasts show that QPF is generally improved out to 6–12 h when all-sky IR BTs are assimilated (see section 4 for more details). Therefore, for PRECIP2021 and “PRE”-CIP2021, the size of the ensemble was reduced from 40 to 20 after the first 12 h, providing a combination of 40-member 12-h ensemble forecasts and 20-member 48-h ensemble forecasts for each run. Clark et al. (2011) and Schwartz et al. (2014, 2019) showed that ensemble forecasts with 10–20 members can adequately quantify the uncertainties associated with the forecasts.

The real-time data assimilation and forecast experiments for PRECIP2021 (Taiwan) and “PRE”-CIP2021 (Colorado)

will be referred to as RT2021TW and RT2021CO, respectively. To facilitate similar verifications on the impact of assimilating all-sky IR BTs, we also performed retrospective “NoIR2021CO” runs. Different from the NoIR2020 runs, the NoIR2021CO runs implemented both domains of RT2021CO to properly resolve the circulations of localized convective storms that are frequently observed during the “PRE”-CIP2021 period in the United States, and for “PRE”-CIP2021 we will only evaluate the 3-km forecasts. Since NoIR2020 can be used to evaluate the potential impacts of all-sky IR on the rainfall forecast during the East Asian summer monsoon, we decided not to perform NoIR2021TW due to limited computational resources, and RT2021TW will not be evaluated in this current study. Both RT2021CO and NoIR2021CO were initialized twice daily at 0000 and 1200 UTC from 15 July to 15 August 2021 (33 days and 66 forecasts in total). Combined with RT2020 and NoIR2020 from PRECIP2020, they will provide more comprehensive evaluations on the impacts of assimilating all-sky IR BTs with two different regions at two different years.

3. Verification metrics

Two datasets are used to evaluate the impact of assimilating all-sky IR BTs on QPF. For the 9-km PRECIP2020 forecasts of RT2020 and NoIR2020, we use the $0.1^\circ \times 0.1^\circ$ Integrated Multi-satellite Retrievals for GPM (IMERG; Huffman et al. 2019) rainfall estimates produced by the Global Precipitation Measurement (GPM) project that combines multiple microwave sensors from the GPM constellation satellites, as well as all-sky infrared radiances and surface rain gauges. Although certain deficiencies exist (e.g., Lee et al. 2019; Chen et al. 2022b), IMERG is one of the most reliable estimations of global precipitation with high spatiotemporal resolutions and seamless coverage over both land and sea. For the 3-km “PRE”-CIP2021 forecasts of RT2021CO and NoIR2021CO, we use the Stage-IV rainfall estimates (Lin and Mitchell 2005), which have a 4-km grid spacing and are generated by the NCEP’s Environmental Modeling Center (EMC) using ground-based radars and rain gauges. In addition to QPF verifications, rawinsonde observations from the MADIS are used to evaluate the forecasts of large-scale environments. Due to the requirement of the workflow of the real-time system, no rawinsonde observations are assimilated for the last EnKF cycles (at 0000 or 1200 UTC) because these observations came in much later than the time required to provide the ensemble forecasts, therefore the ensemble forecasts at 0-h forecast lead time (identical to the analysis of the last EnKF cycle at 0000 or 1200 UTC) are independent of verified rawinsondes. The WRF outputs are interpolated to the IMERG or Stage-IV grid and rawinsonde locations using linear interpolation.

The primary focus of this study is QPF, which is evaluated using the equitable threat score (ETS; Wilks 2011), the area under the receiver operating characteristic (ROC) curve (AUC; Marzban 2004), and the fraction skill score (FSS; Roberts and Lean 2008). Information from the entire ensemble is used in the calculations of all three metrics.

ETS is a pointwise, deterministic metric, with higher scores representing more accurate forecasts. Using a 2×2 contingency

table that determines the hits, misses, and false alarms of a deterministic forecast compared with the observations, ETS is formulated as

$$\text{ETS} = \frac{\text{hits} - \text{hits}_{\text{random}}}{\text{hits} + \text{misses} + \text{false alarms} - \text{hits}_{\text{random}}},$$

where $\text{hits}_{\text{random}} = (\text{hits} + \text{misses}) \times (\text{hits} + \text{false alarms}) / \text{total events}$ represents the reference value of hits for a completely random forecast. To include the information from the entire ensemble, the probability-matched mean (PMM; Ebert 2001) is used to calculate ETS instead of the arithmetic mean. The PMM preserves the cumulative distribution function (CDF) of rainfall of the entire ensemble while keeping the horizontal structure of the ensemble arithmetic mean at the same time, and the arithmetic mean is not able to present the extreme values of the entire ensemble.

AUC is a pointwise, probabilistic metric evaluating the resolution of the forecasts on the occurrence of events exceeding a certain threshold, with higher scores representing better discriminations between events and nonevents. A 2×2 contingency table is first generated considering whether the forecast probability of a certain rainfall amount exceeds a certain probability threshold; this is different from the contingency table for ETS, which considers whether a deterministic forecast exceeds a certain rainfall threshold. Then, the ROC curve is generated by plotting the probability of detection, $\text{hits}/(\text{hits} + \text{misses})$, against the probability of false detection, $\text{false alarms}/(\text{correct negatives} + \text{false alarms})$, for a set of probability thresholds ranging from 0 to 1 using the forecast probability contingency table. Last, AUC is calculated based on the ROC curve using the trapezoidal approximation.

FSS is a neighborhood, probabilistic metric based on neighborhood ensemble probability (NEP; Schwartz and Sobash 2017), with higher scores representing more accurate rainfall forecasts at a certain neighborhood radius (also called the horizontal or spatial scale of a given FSS calculation). NEPs at each grid point given a certain rainfall threshold and a certain neighborhood radius (spatial scale) for the forecasts and the corresponding neighborhood probability (NP; Schwartz and Sobash 2017) of the observations are first calculated, then FSS for a certain combination of rainfall threshold and neighborhood radius is formulated as

$$\text{FSS} = 1 - \frac{\sum_{i=1}^N (\text{NEP}_i^f - \text{NP}_i^o)^2}{\sum_{i=1}^N [(\text{NEP}_i^f)^2 + (\text{NP}_i^o)^2]},$$

where NEP_i^f and NP_i^o represents NEP of the forecasts and NP of the observations at the i th of the total N grid points. A smaller difference between NEP and NP results in a higher FSS value. When a larger neighborhood radius is used, it is more likely for the NEPs of the forecasts and the observations to overlap, therefore FSS often increases with increasing neighborhood radius when the rainfall threshold is fixed.

When calculating ETS, AUC, and FSS, we adopted percentile thresholds that vary with time instead of fixed physical

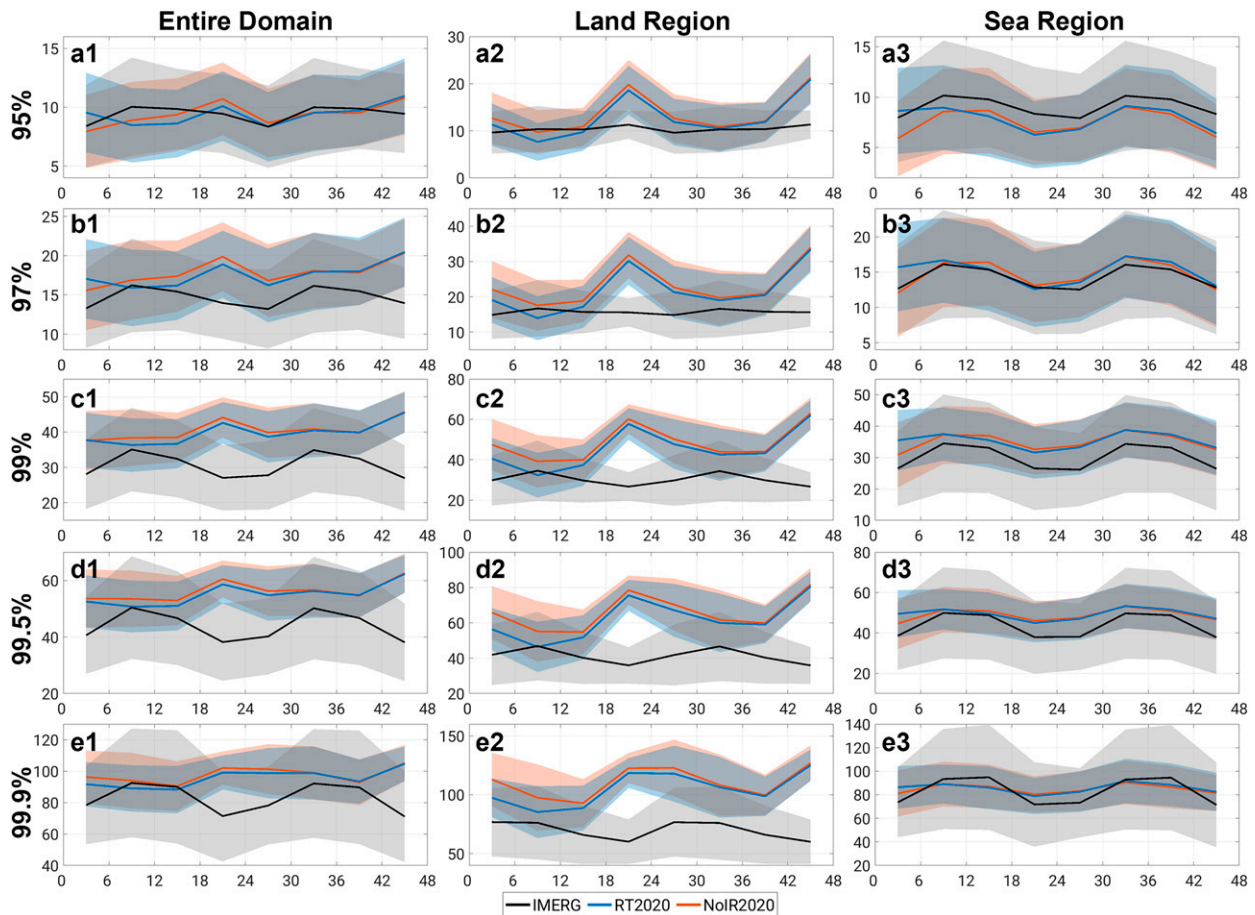


FIG. 2. Distributions of physical thresholds with respect to forecast lead times at the (a) 95th, (b) 97th, (c) 99th, (d) 99.5th, and (e) 99.9th percentiles over (left) the entire domain, (center) the land region, and (right) the sea region. Solid lines are the mean values of the observations or the forecasts. Shadings mark the range of one standard deviation. Values from the entire ensemble are used for the forecasts.

thresholds. The percentile thresholds can help correct some model biases and facilitate verifications that focus on the forecast skills of spatial patterns of given rainfall occurrence frequencies (Dey et al. 2014; Gowan et al. 2018; Schwartz 2019). For each day's forecasts at each forecast lead time, the physical thresholds are established by calculating the 95th, 97th, 99th, 99.5th, and 99.9th percentiles of the rainfall values produced by the entire ensemble, and ETS, AUC, and FSS are calculated against physical thresholds that are similarly established for the IMERG and Stage-IV estimates that cover the same region of the verified model domain. For ETS, because PMM preserves the rainfall CDF of the entire ensemble, the physical values of PMM's percentiles are identical to those of the entire ensemble.

Environmental conditions are evaluated using root-mean-square errors (RMSEs) and ensemble standard deviations (STDs). RMSEs are verified against rawinsonde observations, and STDs are calculated against the ensemble mean. Smaller RMSEs indicate smaller errors, while STDs that are comparable to the corresponding RMSEs—neither too large nor too small—suggest that the ensemble spread adequately represents the uncertainty of the atmosphere.

We use the Wilcoxon signed rank test (Wilks 2011) for the statistical significance test, which does not assume any specific form of the distributions. For each rainfall threshold and/or forecast lead time, we first calculate the differences between the abovementioned metrics obtained using RT forecasts and NoIR forecasts (we focus more on the one-on-one paired differences between these two forecasts, rather than the differences between their overall distributions), then we apply the Wilcoxon signed rank test to the collected differences (with sample sizes of 83 for PRECIP2020, i.e., RT2020 and NoIR2020, and 66 for “PRE”-CIP2021, i.e., RT2021CO and NoIR2021CO) to examine whether these differences are statistically significantly greater or smaller than 0. All statistical significance tests are performed for the 95% and 99% confidence levels.

Due to the significant computational costs to run CRTM and limited storage space that requires the outputs of the ensemble forecasts to be postprocessed shortly after they are generated to keep only the most essential model fields, no systematic verifications of simulated IR BTs against AHI or ABI observations are performed.

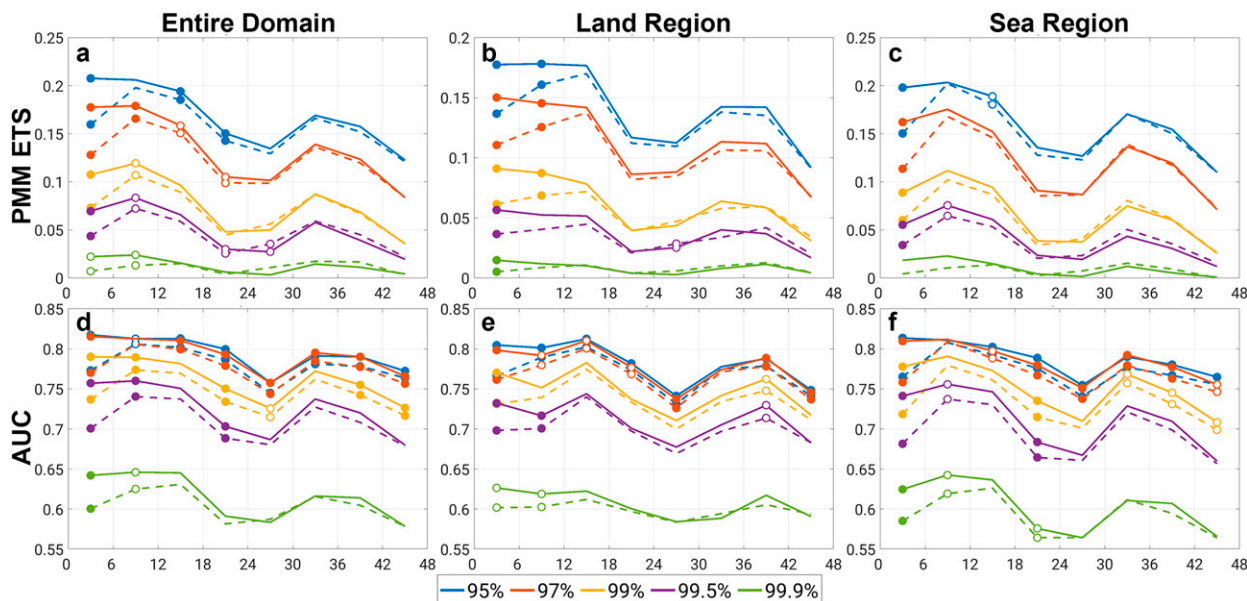


FIG. 3. (a)–(c) ETS of the PMM and (d)–(f) AUC for the PRECIP2020 experiments over (left) the entire domain, (center) the land region, and (right) the sea region. Solid and dashed lines represent scores of RT2020 and NoIR2020, respectively. Open circles and filled circles indicate that the differences between the two experiments' scores are statistically significant at the 95% and 99% confidence levels, respectively.

4. PRECIP2020 verification

We first present the evaluations of the forecasts during the PRECIP2020 experiments in the East Asia and western North Pacific region, namely, RT2020 and NoIR2020 forecasts. All the results in this section are obtained using the forecasts from the 9-km outer domain.

Figure 2 shows the distributions of physical thresholds at different percentiles with respect to forecast lead times for the RT2020 and NoIR2020 forecasts and the IMERG estimates. The mean values of the physical thresholds of RT2020 and NoIR2020 are comparable with those of IMERG at the 95th percentile (Fig. 2a1), but they become higher than the IMERG's physical values when moving toward higher percentiles, suggesting a slight overprediction of rainfall at these percentiles (Figs. 2b1–e1). An outstanding characteristic is the offset of the diurnal cycles in the forecasts' physical thresholds compared with those from IMERG. If we divide the model domain into the land region and the sea region, calculate the physical thresholds of the percentiles within each region, and compare the temporal evolutions of the forecasts' physical thresholds at these two regions with the corresponding IMERG thresholds at these two regions, it is apparent that the forecasts generally have a good match with IMERG (both diurnal cycles and magnitudes of the thresholds) at the sea region (Figs. 2a3–e3), while notable discrepancies occur at the land region (Figs. 2a2–e2). At the land region, the 18–24- and 42–48-h forecast diurnal peaks correspond to the local afternoon of 0600–1200 UTC (for Taiwan, local time = UTC + 8 h), while the 6–12- and 30–36-h IMERG diurnal peaks correspond to the local late night to the early morning of 1800–0000 UTC. This late night to early morning rainfall

peak is frequently observed in the coastal regions of East Asia (Chen et al. 2009; Xu and Zipser 2011). It is often associated with land–sea breezes, low-level/boundary layer jets, and their interactions (Chen et al. 2016; Du and Rotunno 2018; Du and Chen 2019), and the numerical models nowadays still lack sufficient skills in simulating these mechanisms even with convection-permitting grid spacings, resulting in unsatisfactory skills in forecasting late night to early morning rainfall (e.g., Huang et al. 2022; Lu et al. 2022). The necessary horizontal and vertical resolution to accurately capture this late-night to early-morning rainfall peak in East Asian coastal regions still deserves further studies.

Using percentile thresholds can partly mitigate these systematic model biases. RT2020 forecasts show generally higher ETSs than NoIR2020 forecasts for the first 24 h, although their differences diminish with the increasing forecast lead time or the increasing percentile threshold (Fig. 3a). These improvements are significant at the 99% confidence level for all percentiles except for the 99.9th percentile at the first 6 h, and significant at least at the 95% confidence level except for the 95th percentile at 6–12 h (Fig. 3a). The improvements last slightly longer at the land region (improvements significant at the 99% confidence level for percentiles up to the 99th for 6–12 h; Fig. 3b) than the sea region (mostly improvements are only significant for 0–6 h; Fig. 3c). Additionally, RT2020s AUCs are higher than those of NoIR2020 and are significant for most percentile thresholds for 0–12 h; the significance also extends to 48 h for the 95th and 97th percentiles (Figs. 3d–f). This suggests that the RT2020 forecasts better discriminate the rainfall occurrence than the NoIR2020 forecasts, and the improvements can be further extended with additional calibrations and bias corrections

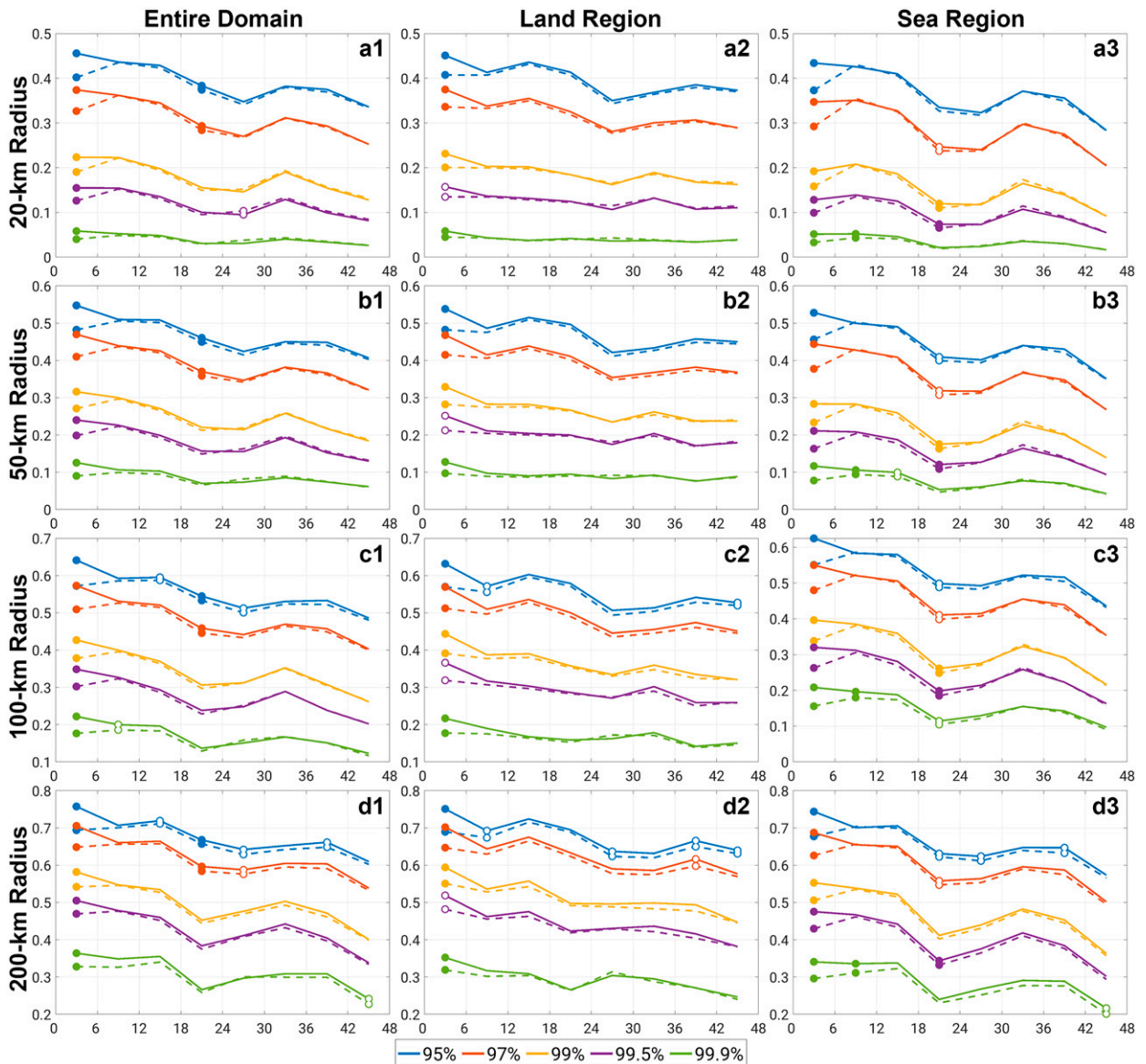


FIG. 4. FSS for the PRECIP2020 experiments with a neighborhood radius of (a) 20, (b) 50, (c) 100, and (d) 200 km over (left) the entire domain, (center) the land region, and (right) the sea region. Solid and dashed lines represent scores of RT2020 and NoIR2020, respectively. Open circles and filled circles indicate that the differences between the two experiments' scores are statistically significant at the 95% and 99% confidence levels, respectively.

(although percentile thresholds already serve as crude bias correction processes).

As previously explained, ETS and AUC are both pointwise metrics. Neighborhood verifications using FSS suggest that the assimilation of all-sky IR BTs improves short-term rainfall forecasts at both small and large spatial scales (neighborhood radii) too: similar to ETS and AUC, RT2020s FSSs are higher than those of NoIR2020 for 0–6-h rainfall forecasts for all percentile thresholds at all horizontal scales from 20 to 200 km, regardless of whether it is over the land region or the sea region (Fig. 4). Almost all these multiscale improvements at 0–6-h lead time are significant at the 99% confidence level (only a few at 95% level).

Besides improved rainfall forecasts, RT2020 forecasts also represent the environments and their uncertainties better than the NoIR2020 forecasts. Statistically significant reductions in RMSEs (at the 99% confidence level) occur for temperature and dewpoint (Figs. 5a,b) in the RT2020 forecasts compared with the NoIR2020 forecasts. For the wind fields (Figs. 5c,d), it is noted that the error at 0-h forecast lead time (i.e., final EnKF analysis) is statistically significantly increased for U wind in the RT2020 forecasts (Fig. 5c). Some recent studies also suggest that assimilating all-sky IR BTs might slightly degrade large-scale circulations in the analysis (Hartman et al. 2023). However, RT2020s RMSEs of wind fields become statistically

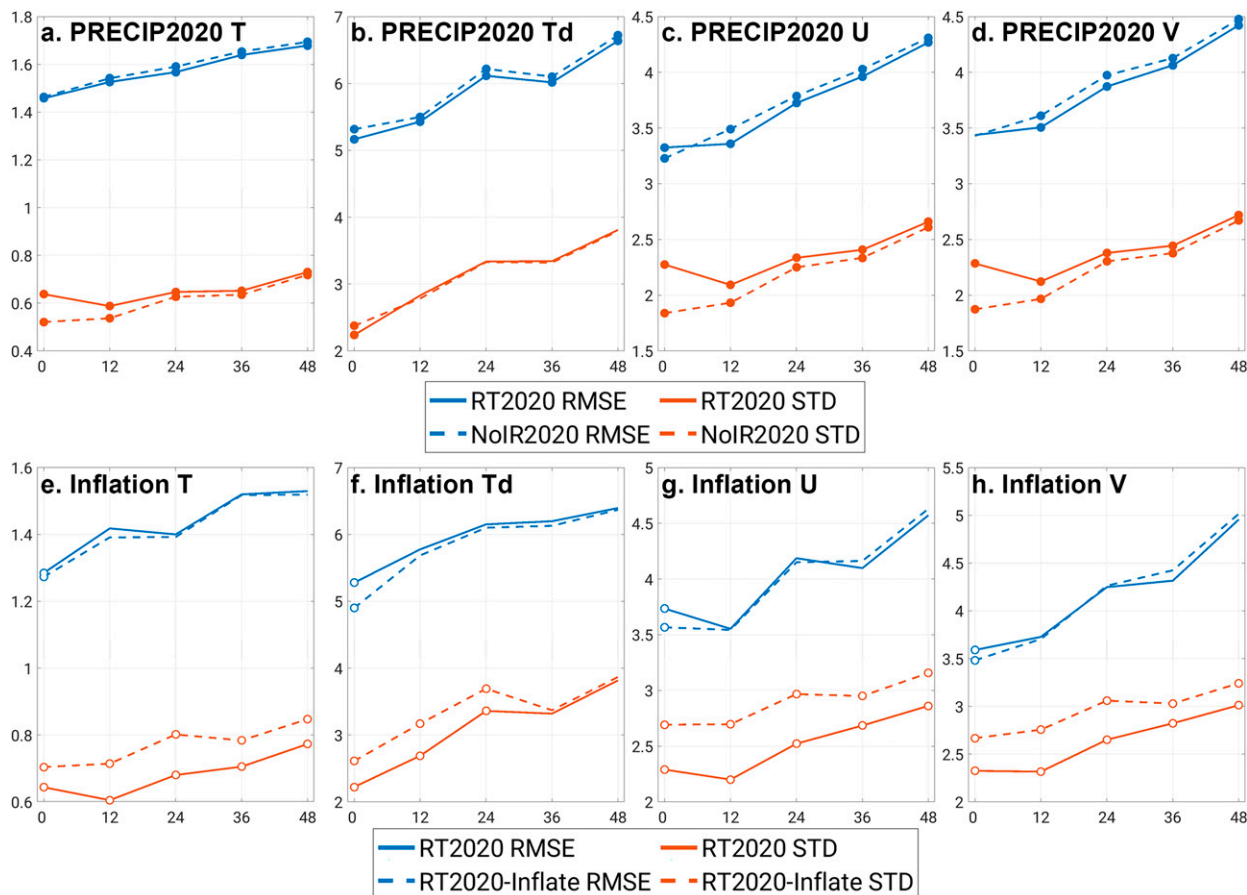


FIG. 5. Comparisons of RMSEs and STDs for (a),(e) T , (b),(f) T_d , (c),(g) U , and (d),(h) V between (top) the RT2020 and NoIR2020 forecasts, and (bottom) the RT2020-Inflate and corresponding RT2020 forecasts that cover the same period. Open circles and filled circles indicate that the differences between the two experiments' scores are statistically significant at the 95% and 99% confidence levels, respectively.

significantly lower than NoIR2020 beyond 12 h (at the 99% confidence level). This improvement of the environments spanning the entire 48-h forecast period also extends across the entire troposphere (Figs. 6a–d). Consistent with the overall average shown in Fig. 5, at 0 h, the RT2020s RMSEs in temperature and V wind component are generally mixed with improvements and degradations compared with NoIR2020s RMSEs, while for the U wind component RT2020s RMSEs are generally higher than those of NoIR2020. However, RT2020s RMSEs become overwhelmingly lower than those of NoIR2020 beyond 12 h across the entire troposphere with only occasional degradations. This suggests that although the improvements to rainfall forecasts resulting from assimilating all-sky IR BTs are generally limited to the first 6–12 h, the improvements to the environments last longer.

RT2020 forecasts also provide statistically significant enhancement in ensemble STDs (at the 99% confidence level) compared with the NoIR2020 forecasts (Figs. 5a–d), except for the dewpoint which is only significant at 0 h. The greater STDs in RT2020 forecasts also extend throughout the entire troposphere (Figs. 6e–h), except for a reduction in STDs at the upper troposphere for dewpoint (Fig. 6f). Although the algorithms of

EnSRF make the ensemble spread smaller when more observations are assimilated, RT2020 forecasts have stronger and more active updrafts and downdrafts compared with NoIR2020 (figure not shown), and the enhanced deep convective activities in RT2020 forecasts can lead to their greater ensemble spread. When comparing STDs with RMSEs, STDs of both RT2020 and NoIR2020 forecasts are smaller than their corresponding RMSEs, suggesting that the ensemble forecasts are underdispersive, which is an issue commonly observed in ensemble forecasts using a regional model (e.g., Schumacher and Clark 2014; Schwartz et al. 2014; Hagelin et al. 2017). Nonetheless, due to the smaller RMSEs and larger STDs in the RT2020 forecasts, it is less underdispersive than the NoIR2020 forecasts. This indicates that the RT2020 forecasts better capture the uncertainty of the atmospheric states than the NoIR forecasts.

As mentioned in section 2, we added SKEP, SPPT, and multiplicative covariance inflation in the real-time forecasts of PRECIP2021 to combat the underdispersive ensemble forecasts. Although RT2021TW forecasts show notably larger STDs than RT2020 forecasts (figure not shown), this is not a fair comparison because the synoptic activities in these two years are different from a climate perspective. Therefore, for 6 days of

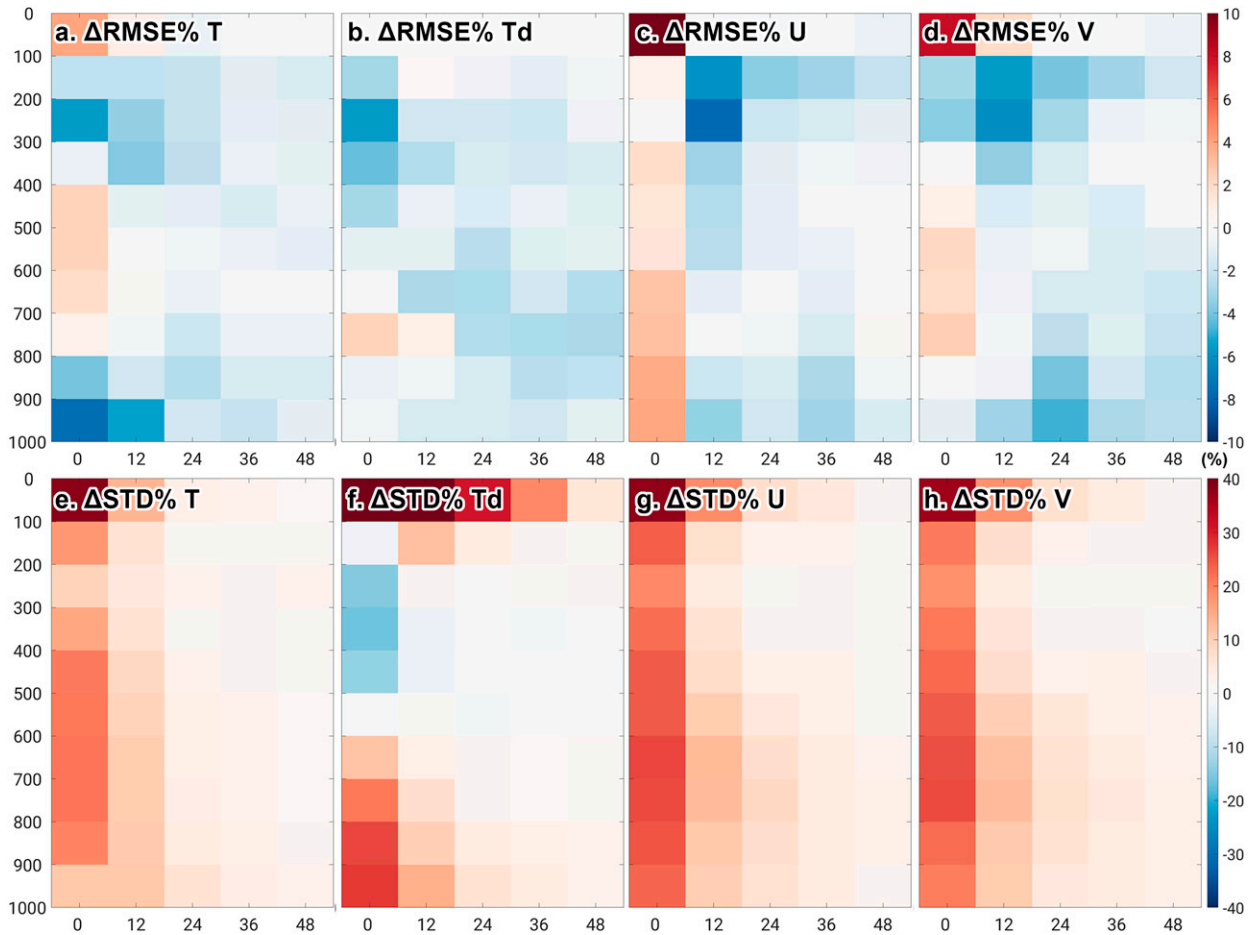


FIG. 6. Vertical distribution of relative changes (in percentage) of (top) RMSEs and (bottom) STDs of the RT2020 forecasts with respect to the NoIR2020 forecasts for (a),(e) T , (b),(f) T_d , (c),(g) U , and (d),(h) V .

4–9 July 2020 when Kyushu, Japan, was hit by devastating heavy rainfall, we rerun the RT2020 forecasts with SKEB, SPPT, and multiplicative covariance inflation (referred to as “RT2020-Inflate” hereafter; only 9-km domain is used so that the results are consistent with the rest of this section). Figures 5e–h and 7 show the changes in RT2020-Inflate’s RMSEs and STDs relative to those from RT2020 that cover the same period. It is apparent that applying these methods leads to overwhelming STD increases throughout the entire 48-h forecast periods (Figs. 5e–h) and this behavior persistently occurs for all 6 days of forecasts, except for occasional STD decreases beyond 36 h in dewpoint temperature (Figs. 5f and 7f) and one forecast in V wind component (Fig. 7h). In the meantime, RMSEs of RT2020-Inflate are also slightly lower than those of RT2020 at 0-h forecast (i.e., final EnKF analysis), although for forecast beyond 12 h they present no difference (Figs. 5e–h and 7a–d). The persistent STD increases at all variables in almost all forecast days in this short-period sensitivity test suggest that these methods helped to maintain a more reasonable ensemble spread as expected. Given the formulation of EnKF that the analysis will be closer to the observations with greater background ensemble spread, the reduced

RMSEs are also not surprising, even though the observations used for verifications are not assimilated.

5. “PRE”-CIP2021 verifications

This section presents the evaluations of the forecasts during the “PRE”-CIP2021 experiments in Colorado, namely, RT2021CO and NoIR2021CO. All the results in this section are obtained using the forecasts from the 3-km, convection-permitting inner domain. Since most improvements in rainfall forecast appear during the first 12 h, we have also provided a different version of Figs. 8–11 with the first 12 h stretched in the online supplemental material as Figs. S1–S4.

Figure 8 shows the distributions of the percentile thresholds’ physical values for the “PRE”-CIP2021 experiments, as well as the values established separately for the 0000 and 1200 UTC forecasts. Overall, the physical values of the forecasts are in good agreement with those from Stage-IV. NoIR2021CO tends to produce more rainfall for the first 12 h compared with Stage-IV, but this overprediction is partly mitigated in RT2021CO. The onset of diurnal rainfall in RT2021CO and NoIR2021CO also tends to be slightly later (~ 1 h) than

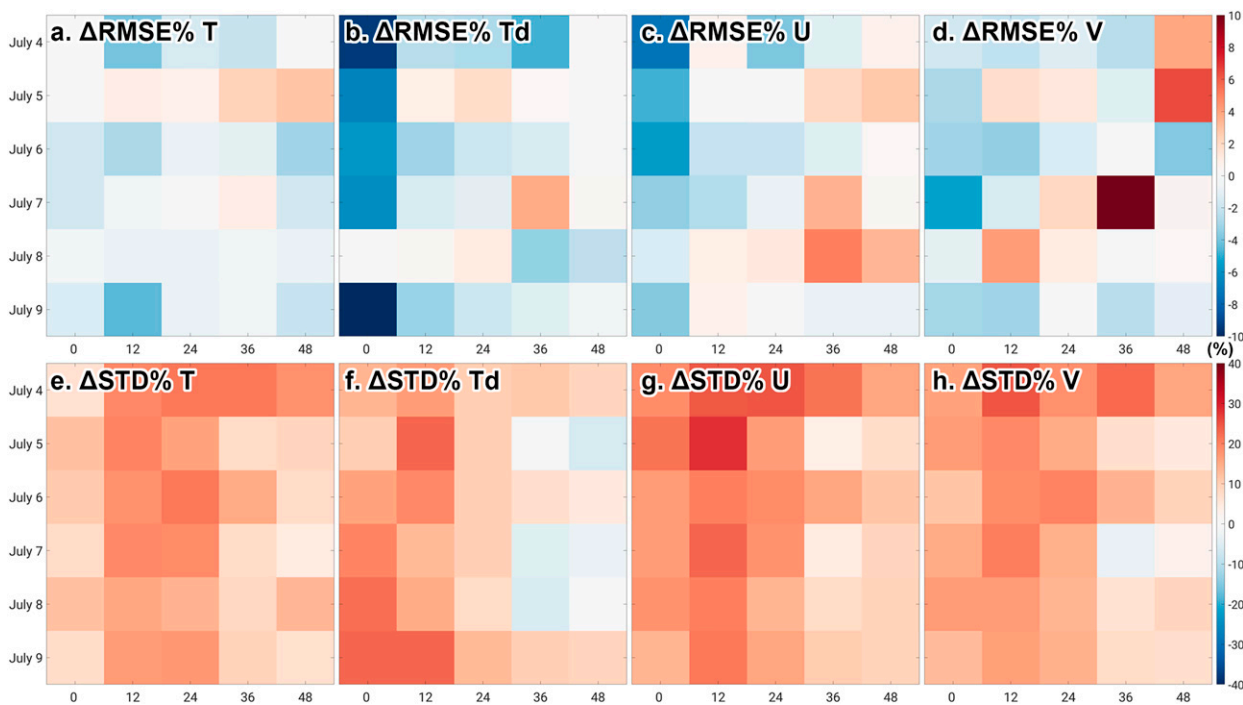


FIG. 7. Day-by-day relative changes (in percentage) of (top) RMSEs and (bottom) STDs of the RT2020-Inflate forecasts with respect to the RT2020 forecasts that cover the same period for (a),(e) T , (b),(f) T_d , (c),(g) U , and (d),(h) V .

that in Stage-IV at the 95th and 97th percentiles (Figs. 8a,b), but this delay disappears at higher percentile thresholds. Figure 8 also shows that occasionally some percentile's mean values, or even the upper quartile values, become zero. This is because very little rainfall is observed or predicted in the 3-km domain, particularly in the late night to morning hours (12–18- and 36–42-h lead times for the 0000 UTC forecasts, and 0–6- and 24–30-h lead times for the 1200 UTC forecasts). Therefore, we calculated the number of days that a certain percentile threshold becomes zero, and they are shown in Fig. 9. Note that there are 33 forecasts for both the 0000 and 1200 UTC forecasts. Therefore, when the number of zero-value threshold days for a given percentile at a given forecast lead time reaches 33, there is no forecast within the entire “PRE”-CIP2021 period that this given percentile exceeds 0 mm at this forecast lead time. We can see a steady increase in the number of zero-value threshold days for all percentiles, starting from the early night and peaking around noon, both in the observations (Figs. 9a,b) and in the forecasts (Figs. 9c–f). The forecasts have fewer zero-value threshold days than the observations. Nonetheless, if a certain percentile threshold equals zero at a certain forecast lead time either in the observations or in the forecasts, this forecast at this particular time must be excluded in ETS, AUC, and FSS calculations, because a physical value of zero no longer represents the corresponding percentile threshold. This will lead to a much smaller sample size—or even complete removal of all forecasts—at certain times.

Figure 10 shows the ETSs and AUCs for all forecasts from the “PRE”-CIP2021 experiment, as well as calculated separately for the 0000 and 1200 UTC forecasts using

their percentiles. Consistent with evaluations in section 4 for PRECIP2020, RT2021CO forecasts have higher ETS than NoIR2021CO for the first 2–8 h, with the first 2–4 h achieving at least the 95% confidence level of statistical significance (Fig. 10a). If we examine only the 0000 UTC forecasts, there are consistent 0–4-h statistically significant improvements in ETS except for the 99.9th percentile (Fig. 10b). For the 1200 UTC forecasts, the sample sizes at the beginning of the forecasts are too small (Fig. 9b), making the improvements in RT2021CO compared with NoIR2021CO in the first 2–3 h unreliable (Fig. 10c). For AUC, RT2021CO forecasts are generally higher for the first 6–18 h (Fig. 10d). If we examine only the 0000 UTC forecasts, RT2021CO's AUCs show statistically significant improvements at the 95%–99% confidence levels for the first 4–6 h compared with NoIR2021CO's AUCs (Fig. 10e), suggesting that we can further improve the performance of RT2021CO forecasts with adequate calibrations and bias corrections.

The FSSs for the “PRE”-CIP2021 experiment in Fig. 11 generally show characteristics that are consistent with ETSs and AUCs. When all forecasts are aggregated together, RT2021CO forecasts show significantly higher FSSs than NoIR2021CO forecasts for the first 3–6 h (Figs. 11a1–d1), depending on the percentile and the spatial scale (neighborhood radius). If we only consider the 0000 UTC forecasts, RT2021CO forecasts significantly outperform NoIR2021CO forecasts for the first 4–6 h, with the majority of the statistical significance tests exceeding the 99% confidence level (Figs. 11a2–d2). RT2021CO's 1200 UTC forecasts also show slightly higher FSSs for the first 2–3 h than those in

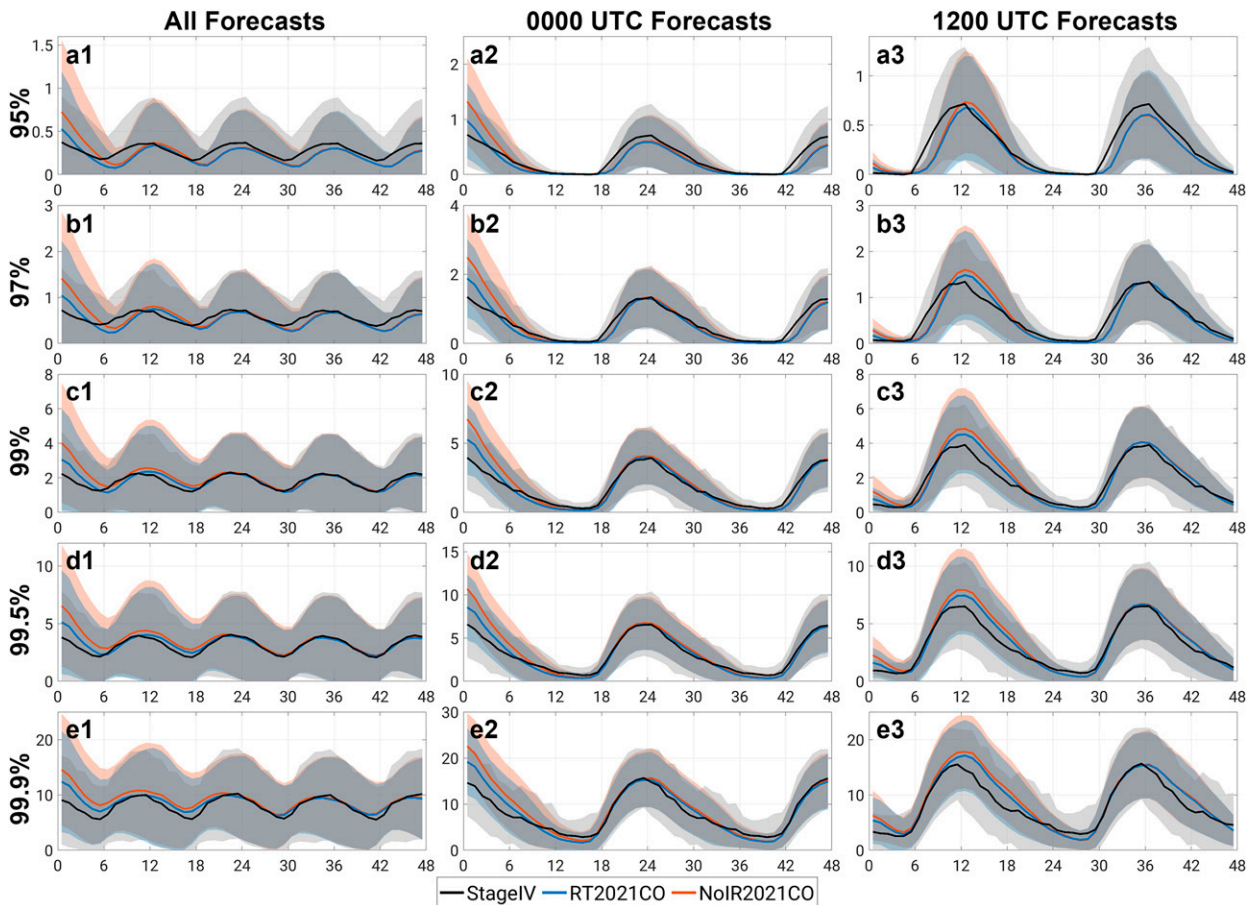


FIG. 8. As in Fig. 2, but for the “PRE”-CIP2021 experiments containing (left) all forecasts, (center) only 0000 UTC forecasts, and (right) only 1200 UTC forecasts.

NoIR2021CO (Figs. 11a3–d3), but the sample size is too small to draw any conclusions.

The number of rawinsonde stations within the 3-km “PRE”-CIP2021 domain is much smaller than that within the 9-km PRECIP2020 domain (8 versus 70–80). There are also very few observations available below 900 hPa considering the topography of this domain, therefore RT2021CO and NoIR2021CO’s differences in RMSEs and STDs below 900 hPa should be examined with caution. In general, RT2021CO’s RMSEs are slightly lower than those of NoIR2021CO, although these differences are only occasionally statistically significant at the 95% or 99% confidence levels (Fig. 12). Temperature and dewpoint generally exhibit slightly reduced RMSEs in RT2021CO compared with NoIR2021CO across the whole troposphere (Figs. 13a,b), while for U and V wind components the RMSE changes are more mixed (Figs. 13c,d). On the other hand, we still see overall significantly increased STDs in RT2021CO compared with NoIR2021CO throughout the entire 48-h forecast period (Fig. 12) and the entire troposphere (Figs. 13e–h), with the only exception being dewpoint at 0 h (final EnKF analysis; Fig. 12b) primarily at the upper troposphere (Fig. 13f). This slight reduction of dewpoint STDs at the final EnKF analysis at the upper troposphere when

all-sky IR BTs are assimilated is also observed in the verifications for PRECIP2020 (Fig. 6f) and the reason deserves further studies.

6. Conclusions

During the summers of 2020 and 2021, the PSU WRF-EnKF data assimilation and forecast system was run in real-time in support of the Prediction of Rainfall Extremes Campaign In the Pacific (PRECIP), assimilating all-sky infrared radiances from the *Himawari-8* geostationary satellite of Japan and the *GOES-16* satellite of the United States, and provided ensemble forecasts every day for weather briefing and discussions of the field campaign. By comparing with retrospective forecasts excluding all-sky infrared radiances in the EnKF data assimilation cycles, this study presents the first systematic evaluation of the impact of assimilating all-sky infrared radiances for the quantitative precipitation forecasts (QPF) using real-time ensemble forecasts over several seasons at different regions.

Pointwise metrics of equitable threat score (ETS) and area under the receiver operating characteristic (ROC) curve (AUC) as well as neighborhood metric of fraction skill score

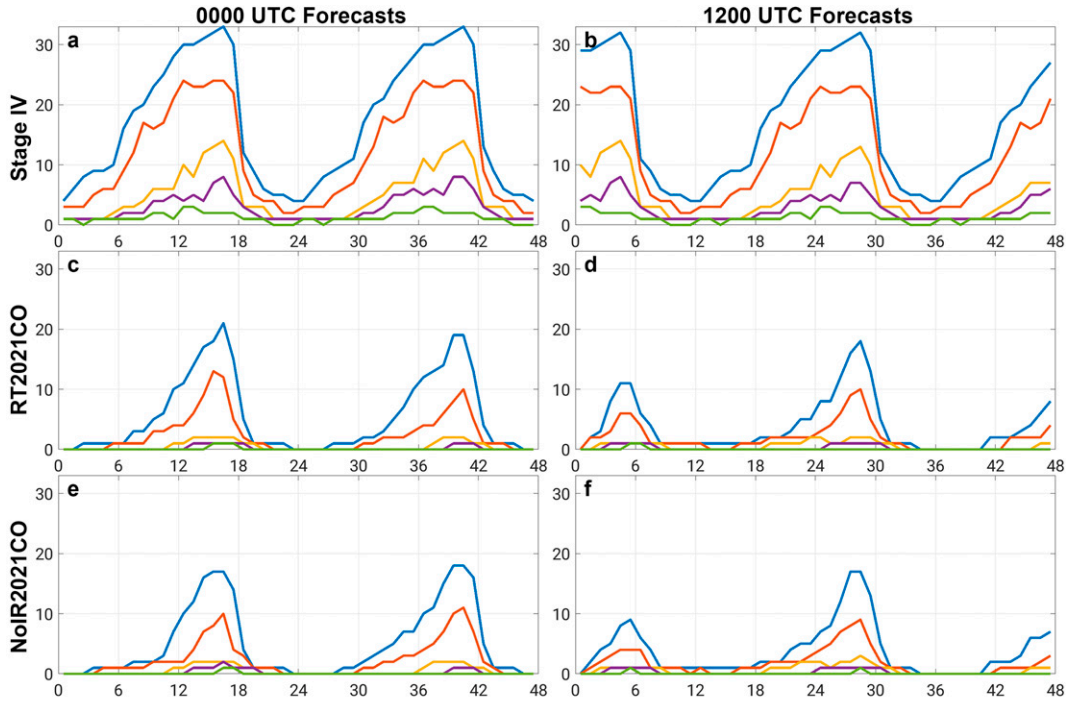


FIG. 9. Number of days that the physical value of a given percentile threshold equals zero for (a),(b) Stage-IV estimates, (c),(d) RT2021CO forecasts, and (e),(f) NoIR2021CO containing (left) only the 0000 UTC forecasts, and (right) only the 1200 UTC forecasts.

(FSS) indicate that the rainfall forecasts are improved for at least 4–6-h lead time when all-sky infrared radiances are assimilated for different rainfall percentile thresholds and spatial scales (neighborhood radii). The 2020 summer forecasts in East Asia and west Pacific also show 6–12-h QPF improvements for

some thresholds. This time scale of 6–12 h of rainfall forecast improvements is similar to what can be achieved with the assimilation of observations from Doppler weather radars (e.g., Xiao and Sun 2007; Aksoy et al. 2010; Clark et al. 2012; Johnson et al. 2015; Surcel et al. 2015; Yussouf et al. 2016;

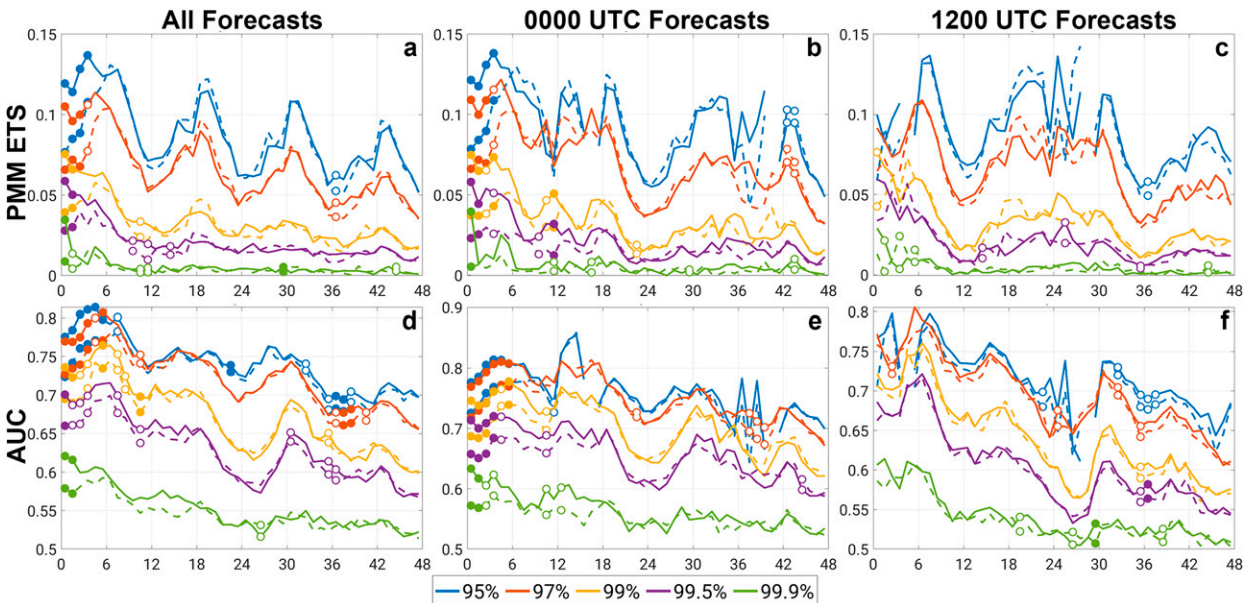


FIG. 10. As in Fig. 3, but for the “PRE”-CIP2021 experiments containing (left) all forecasts, (center) only 0000 UTC forecasts, and (right) only 1200 UTC forecasts.

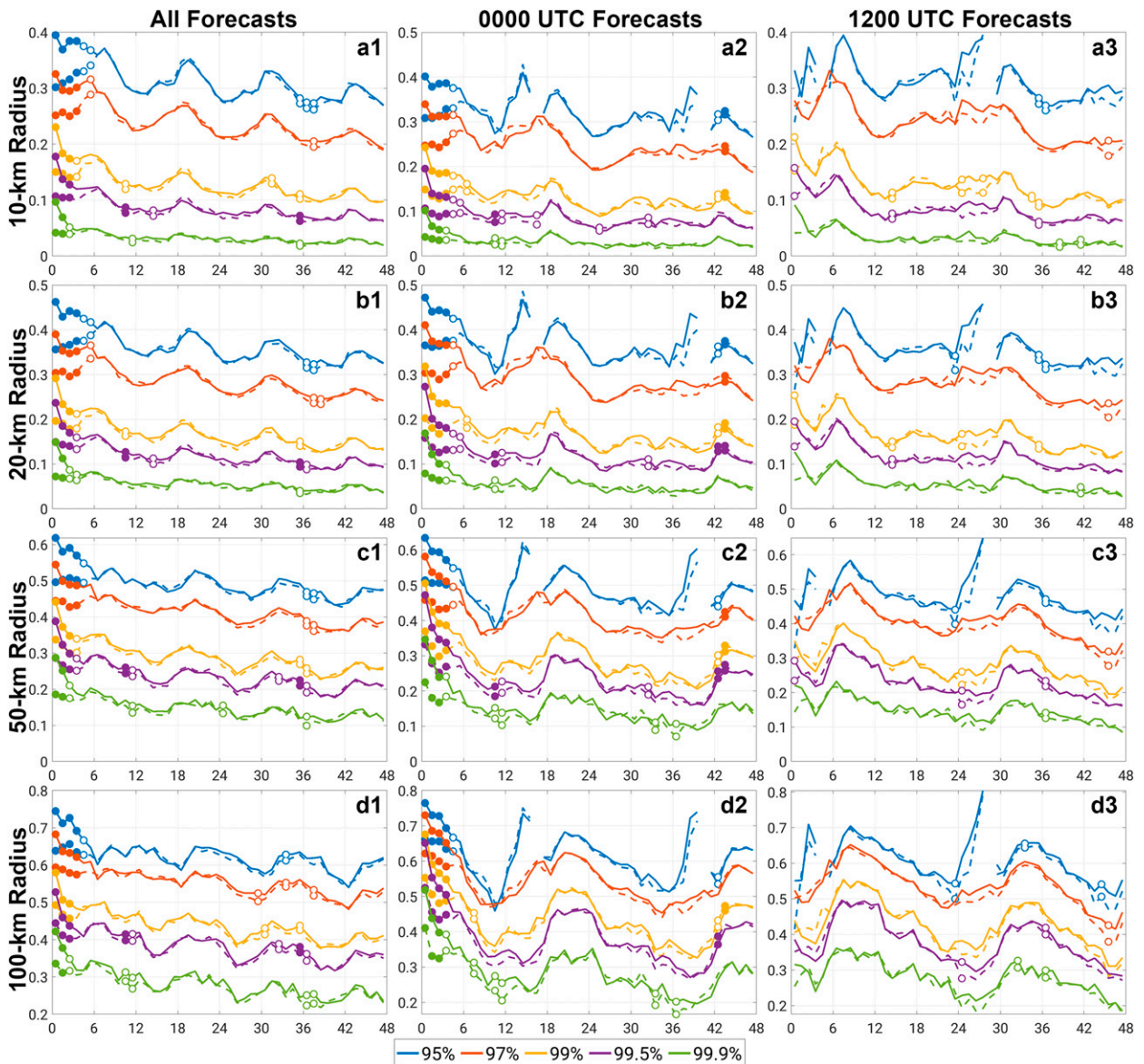


FIG. 11. FSS for the “PRE”-CIP2020 experiments with a neighborhood radius of (a) 10, (b) 20, (c) 50, and (d) 100 km for (left) all forecasts, (center) only 0000 UTC forecasts, and (right) only 1200 UTC forecasts. Solid and dashed lines represent scores of RT2021CO and NoIR2021CO, respectively. Open circles and filled circles indicate that the differences between the two experiments’ scores are statistically significant at the 95% and 99% confidence levels, respectively.

Schwartz et al. 2021), and also likely governed by the limited predictability of convective-to-mesoscale systems (e.g., Y. Zhang et al. 2016, 2022b). The large-scale environments are also improved when all-sky infrared radiances are assimilated, verified against available, independent rawinsonde observations that the RMSEs are generally reduced throughout the entire 48-h forecast period. Furthermore, the ensemble forecasts from EnKF analyses assimilating all-sky infrared radiances contain larger ensemble spreads than when these observations are not assimilated, leading to a better balance between ensemble variance and error and a better representation of the uncertainty of the atmospheric states. The increased ensemble spread extends

throughout the entire troposphere and lasts till the end of the 48-h forecast period. SKEB, SPPT, and multiplicative covariance inflation also help to effectively increase and persistently maintain a more reasonable ensemble spread.

One notable difference when comparing the performance of the PSU WRF-EnKF system during the two years is the smaller and shorter-lasting improvements of assimilating all-sky IR BTs in CONUS (the “PRE”-CIP2021 experiments) when compared with the East Asia and west Pacific (the PRECIP2020 experiments) forecasts. The “PRE”-CIP2021 experiments captured primarily diurnally driven local convective storms as revealed by the apparent diurnal cycle in their percentile thresholds.

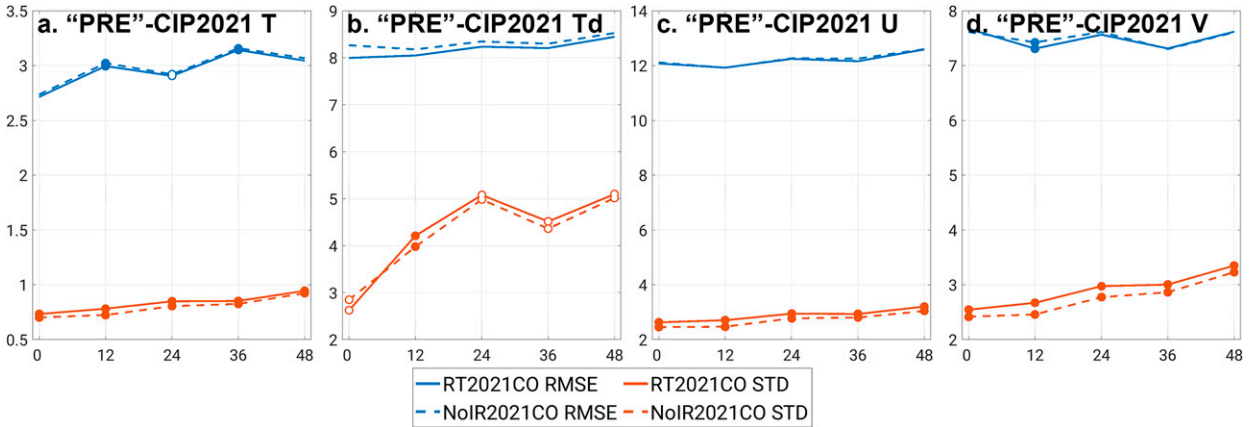


FIG. 12. Comparisons of RMSEs and STDs for (a) T , (b) T_d , (c) U , and (d) V between the RT2021CO and NoIR2021CO forecasts. Open circles and filled circles indicate that the differences between the two experiments' scores are statistically significant at the 95% and 99% confidence levels, respectively.

These convective storms intrinsically have shorter predictability than convection embedded within large-scale mei-yu/baiu fronts that were captured by the PRECIP2020 experiments. The dense surface observations in CONUS might also have

contributed to the less impact of assimilating all-sky IR BTs in the "PRE"-CIP2021 experiments by preconditioning the environment better than the PRECIP2020. Additionally, we did not assimilate other space-borne observations in our system's

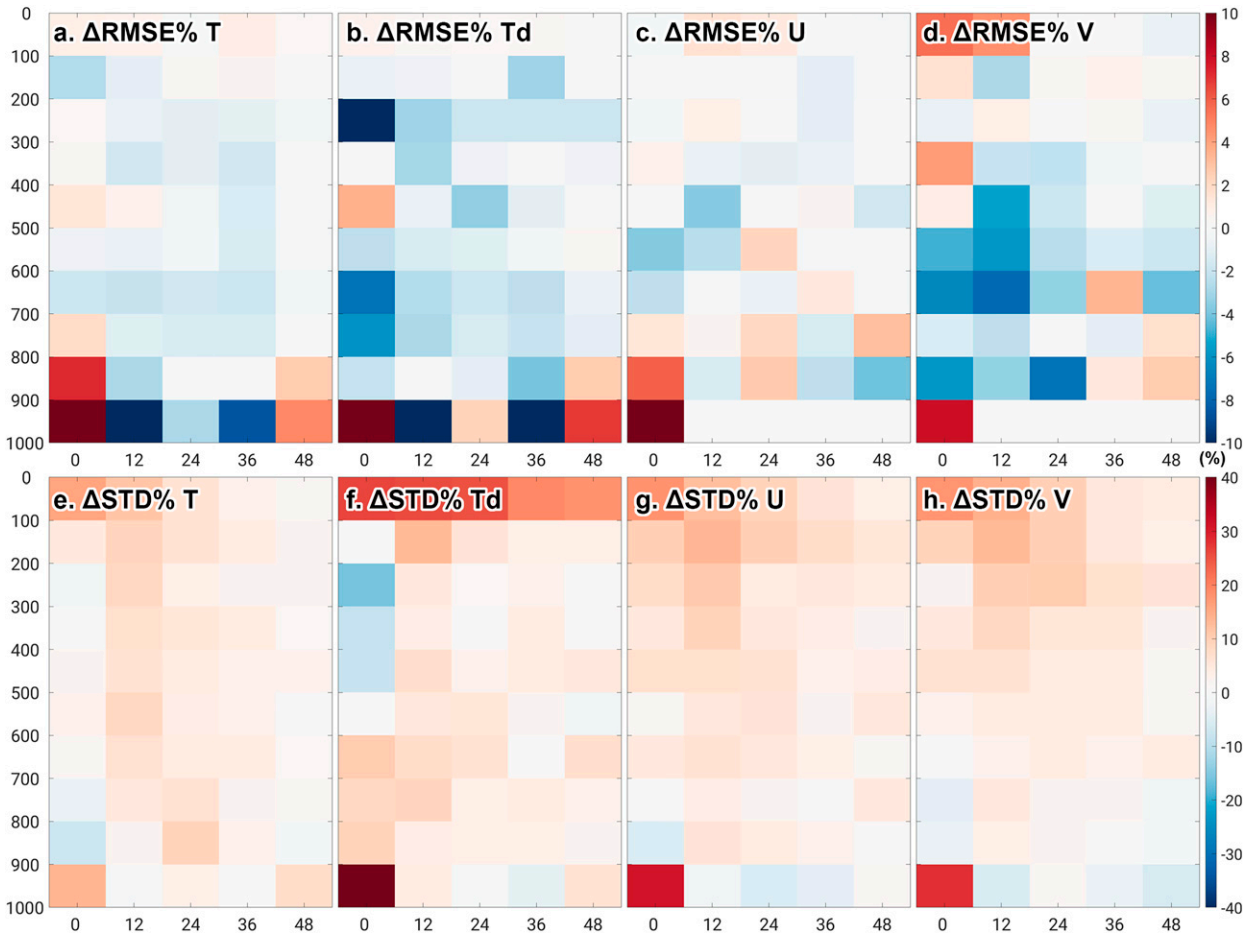


FIG. 13. As in Fig. 6, but for the "PRE"-CIP2021 experiments.

real-time forecasts, such as infrared sounder radiances, all-sky microwave radiances, and derived atmospheric motion vectors (AMVs). Although none of these observations—except for recently developed high-temporal-resolution AMVs (e.g., Zhao et al. 2021)—have the adequate temporal resolution to observe the fast-evolving convective phenomena, the impact of assimilating all-sky IR BTs from geostationary satellites on QPF might be diluted when other space-borne observations are also assimilated. Similar dilutions are also expected when ground-based Doppler weather radar observations are assimilated, although Y. Zhang et al. (2019) suggests that all-sky IR BTs from geostationary satellites—owing to their earlier detection of convection initiation—can still bring in additional benefits compared with ground-based radars based on a case study. Observing system experiments (OSEs) are needed to isolate the influence of conventional observations and other types of remotely sensed observations when they are simultaneously assimilated with all-sky IR BTs from geostationary satellites, which is beyond the scope of this current study.

Last, there are still many remaining issues associated with all-sky IR BT assimilations, such as adequate observation error modeling, treatment of the correlated observation errors, proper covariance localization and simultaneous assimilation of multiple channels, multiscale constraints of the environmental conditions, and the non-Gaussianity of the all-sky observations (e.g., Chan et al. 2020a). Additional studies are still warranted to make better, more efficient, and more effective use of all-sky IR BTs from geostationary satellites. However, considering the overall best spatiotemporal resolution and coverage for the monitoring and prediction of convectively driven rainfall systems compared with other remote sensing platforms, such as infrared and microwave radiances from low-Earth-orbiting satellites and ground-based and airborne Doppler weather radars, the multiyear multiregion evaluation of the real-time ensemble forecasts of the PSU WRF-EnKF system with the assimilation of all-sky IR BTs from the geostationary *Himawari-8* and *GOES-16* satellites presented here demonstrated the tremendous value of these observations in improving short-term QPF. Detailed evaluation of the PRECIP 2022 forecasts using the special field observations collected in East Asia will be reported in a subsequent study.

Acknowledgments. We thank Drs. Rosimar Rios-Berrios (NCAR), James H. Ruppert, Jr. (University of Oklahoma), and many PRECIP participants for their helpful discussions and feedback on the configuration of the PSU WRF-EnKF system and the planning of the real-time modeling for the field campaign, and Dr. Kristen Rasmussen (Colorado State University) for securing the computational resources for the 2022 real-time forecasts. We would also like to thank the three anonymous reviewers, whose comments prominently improved this manuscript. This work is supported by NSF Grants AGS-1712290, AGS-1854607, and AGS-1854559; ONR Grant N000141812517; NOAA NGGPS grant through University of Michigan Subcontract 3004628721; NOAA Grant

NA18OAR4590369; and NASA Grant 80NSSC19K0728. The real-time and retrospective data assimilations and forecasts are performed on the Cheyenne supercomputer (doi:<https://doi.org/10.5065/D6RX99HX>) provided by NCAR's Computational and Information Systems Laboratory (CISL) sponsored by the NSF, and the Stampede 2 supercomputer of the Texas Advanced Computing Center (TACC) through the Extreme Science and Engineering Discovery Environment (XSEDE) program (now the Advanced Cyberinfrastructure Coordination Ecosystem: Services and Support program, or ACCESS) supported by the National Science Foundation (NSF).

Data availability statement. The model output used in this study is subject to the PRECIP data policy, with a restricted release of one year after data generation and public release thereafter (upon request).

REFERENCES

- Aksoy, A., D. C. Dowell, and C. Snyder, 2010: A multicaser comparative assessment of the ensemble Kalman filter for assimilation of radar observations. Part II: Short-range ensemble forecasts. *Mon. Wea. Rev.*, **138**, 1273–1292, <https://doi.org/10.1175/2009MWR3086.1>.
- Anderson, J. L., and S. L. Anderson, 1999: A Monte Carlo implementation of the nonlinear filtering problem to produce ensemble assimilations and forecasts. *Mon. Wea. Rev.*, **127**, 2741–2758, [https://doi.org/10.1175/1520-0493\(1999\)127<2741:AMCIOT>2.0.CO;2](https://doi.org/10.1175/1520-0493(1999)127<2741:AMCIOT>2.0.CO;2).
- Benjamin, S. G., G. A. Grell, J. M. Brown, T. G. Smirnova, and R. Bleck, 2004: Mesoscale weather prediction with the RUC hybrid isentropic-terrain-following coordinate model. *Mon. Wea. Rev.*, **132**, 473–494, [https://doi.org/10.1175/1520-0493\(2004\)132<0473:MWPWTR>2.0.CO;2](https://doi.org/10.1175/1520-0493(2004)132<0473:MWPWTR>2.0.CO;2).
- Buizza, R., M. Milleer, and T. N. Palmer, 1999: Stochastic representation of model uncertainties in the ECMWF ensemble prediction system. *Quart. J. Roy. Meteor. Soc.*, **125**, 2887–2908, <https://doi.org/10.1002/qj.49712556006>.
- Chan, M.-Y., J. L. Anderson, and X. Chen, 2020a: An efficient bi-Gaussian ensemble Kalman filter for satellite infrared radiance data assimilation. *Mon. Wea. Rev.*, **148**, 5087–5104, <https://doi.org/10.1175/MWR-D-20-0142.1>.
- , F. Zhang, X. Chen, and L. R. Leung, 2020b: Potential impacts of assimilating all-sky satellite infrared radiances on convection-permitting analysis and prediction of tropical convection. *Mon. Wea. Rev.*, **148**, 3203–3224, <https://doi.org/10.1175/MWR-D-19-0343.1>.
- Chen, G., W. Sha, and T. Iwasaki, 2009: Diurnal variation of precipitation over southeastern China: Spatial distribution and its seasonality. *J. Geophys. Res.*, **114**, D13103, <https://doi.org/10.1029/2008JD011103>.
- Chen, X., and F. Zhang, 2019: Relative roles of preconditioning moistening and global circumnavigating mode on the MJO convective initiation during DYNAMO. *Geophys. Res. Lett.*, **46**, 1079–1087, <https://doi.org/10.1029/2018GL080987>.
- , —, and K. Zhao, 2016: Diurnal variations of the land-sea breeze and its related precipitation over South China. *J. Atmos. Sci.*, **73**, 4793–4815, <https://doi.org/10.1175/JAS-D-16-0106.1>.
- , O. M. Pauluis, and F. Zhang, 2018: Regional simulation of Indian summer monsoon intraseasonal oscillations at gray-

- zone resolution. *Atmos. Chem. Phys.*, **18**, 1003–1022, <https://doi.org/10.5194/acp-18-1003-2018>.
- , L. R. Leung, Z. Feng, F. Song, and Q. Yang, 2021: Mesoscale convective systems dominate the energetics of the South Asian summer monsoon onset. *Geophys. Res. Lett.*, **48**, e2021GL094873, <https://doi.org/10.1029/2021GL094873>.
- , —, —, and —, 2022a: Crucial role of mesoscale convective systems in the vertical mass, water, and energy transports of the South Asian summer monsoon. *J. Climate*, **35**, 91–108, <https://doi.org/10.1175/JCLI-D-21-0124.1>.
- , —, —, and Q. Yang, 2022b: Precipitation-moisture coupling over tropical oceans: Sequential roles of shallow, deep, and mesoscale convective systems. *Geophys. Res. Lett.*, **49**, e2022GL097836, <https://doi.org/10.1029/2022GL097836>.
- Clark, A. J., and Coauthors, 2011: Probabilistic precipitation forecast skill as a function of ensemble size and spatial scale in a convection-allowing ensemble. *Mon. Wea. Rev.*, **139**, 1410–1418, <https://doi.org/10.1175/2010MWR3624.1>.
- , and Coauthors, 2012: An overview of the 2010 Hazardous Weather Testbed Experimental Forecast Program Spring Experiment. *Bull. Amer. Meteor. Soc.*, **93**, 55–74, <https://doi.org/10.1175/BAMS-D-11-00040.1>.
- Dey, S. R. A., G. Leoncini, N. M. Roberts, R. S. Plant, and S. Migliorini, 2014: A spatial view of ensemble spread in convection permitting ensembles. *Mon. Wea. Rev.*, **142**, 4091–4107, <https://doi.org/10.1175/MWR-D-14-00172.1>.
- Du, Y., and R. Rotunno, 2018: Diurnal cycle of rainfall and winds near the south coast of China. *J. Atmos. Sci.*, **75**, 2065–2082, <https://doi.org/10.1175/JAS-D-17-0397.1>.
- , and G. Chen, 2019: Climatology of low-level jets and their impact on rainfall over southern China during the early-summer rainy season. *J. Climate*, **32**, 8813–8833, <https://doi.org/10.1175/JCLI-D-19-0306.1>.
- Ebert, E. E., 2001: Ability of a poor man's ensemble to predict the probability and distribution of precipitation. *Mon. Wea. Rev.*, **129**, 2461–2480, [https://doi.org/10.1175/1520-0493\(2001\)129<2461:AOAPMS>2.0.CO;2](https://doi.org/10.1175/1520-0493(2001)129<2461:AOAPMS>2.0.CO;2).
- Geer, A. J., and P. Bauer, 2011: Observation errors in all-sky data assimilation. *Quart. J. Roy. Meteor. Soc.*, **137**, 2024–2037, <https://doi.org/10.1002/qj.830>.
- , and Coauthors, 2018: All-sky satellite assimilation at operational weather forecasting centres. *Quart. J. Roy. Meteor. Soc.*, **144**, 1191–1217, <https://doi.org/10.1002/qj.3202>.
- Gowan, T. M., W. J. Steenburgh, and C. S. Schwartz, 2018: Validation of mountain precipitation forecasts from the convection-permitting NCAR ensemble and operational forecast systems over the western United States. *Wea. Forecasting*, **33**, 739–765, <https://doi.org/10.1175/WAF-D-17-0144.1>.
- Hagelin, S., J. Son, R. Swinbank, A. McCabe, N. Roberts, and W. Tennant, 2017: The Met Office convective-scale ensemble, MOGREPS-UK. *Quart. J. Roy. Meteor. Soc.*, **143**, 2846–2861, <https://doi.org/10.1002/qj.3135>.
- Han, Y., P. van Delst, Q. Liu, F. Weng, B. Yan, R. Treadon, and J. Derber, 2006: JCSDA Community Radiative Transfer Model (CRTM): Version 1. NOAA Tech. Rep. NESDIS 122, 40 pp., <https://repository.library.noaa.gov/view/noaa/1157>.
- Hartman, C. M., X. Chen, E. E. Clothiaux, and M.-Y. Chan, 2021: Improving the analysis and forecast of Hurricane Dorian (2019) with simultaneous assimilation of GOES-16 all-sky infrared brightness temperatures and tail Doppler radar radial velocities. *Mon. Wea. Rev.*, **149**, 2193–2212, <https://doi.org/10.1175/MWR-D-20-0338.1>.
- , —, and M.-Y. Chan, 2023: Improving tropical cyclogenesis forecasts of Hurricane Irma (2017) through the assimilation of all-sky infrared brightness temperatures. *Mon. Wea. Rev.*, **151**, 837–853, <https://doi.org/10.1175/MWR-D-22-0196.1>.
- He, J., and Coauthors, 2019: Development and evaluation of an ensemble-based data assimilation system for regional reanalysis over the Tibetan Plateau and surrounding regions. *J. Adv. Model. Earth Syst.*, **11**, 2503–2522, <https://doi.org/10.1029/2019MS001665>.
- Honda, T., and Coauthors, 2018a: Assimilating all-sky Himawari-8 infrared radiances: A case of Typhoon Soudelor (2015). *Mon. Wea. Rev.*, **146**, 213–229, <https://doi.org/10.1175/MWR-D-16-0357.1>.
- , S. Kotsuki, G.-Y. Lien, Y. Maejima, K. Okamoto, and T. Miyoshi, 2018b: Assimilation of Himawari-8 all-sky radiances every 10 minutes: Impact on precipitation and flood risk prediction. *J. Geophys. Res. Atmos.*, **123**, 965–976, <https://doi.org/10.1002/2017JD027096>.
- Hong, S.-Y., Y. Noh, and J. Dudhia, 2006: A new vertical diffusion package with an explicit treatment of entrainment processes. *Mon. Wea. Rev.*, **134**, 2318–2341, <https://doi.org/10.1175/MWR3199.1>.
- Houtekamer, P. L., and H. L. Mitchell, 2001: A sequential ensemble Kalman filter for atmospheric data assimilation. *Mon. Wea. Rev.*, **129**, 123–137, [https://doi.org/10.1175/1520-0493\(2001\)129<0123:ASEKFF>2.0.CO;2](https://doi.org/10.1175/1520-0493(2001)129<0123:ASEKFF>2.0.CO;2).
- Huang, L., Y. Luo, and L. Bai, 2022: An evaluation of convection-permitting ensemble simulations of coastal nocturnal rainfall over South China during the early-summer rainy season. *J. Geophys. Res. Atmos.*, **127**, e2021JD035656, <https://doi.org/10.1029/2021JD035656>.
- Huffman, G. J., and Coauthors, 2019: NASA Global Precipitation Measurement (GPM) Integrated Multi-satellitE Retrievals for GPM (IMERG), version 06. NASA Algorithm Theoretical Basis Doc., 38 pp., https://gpm.nasa.gov/sites/default/files/document_files/IMERG_ATBD_V06.pdf.
- Iacono, M. J., J. S. Delamere, E. J. Mlawer, M. W. Shephard, S. A. Clough, and W. D. Collins, 2008: Radiative forcing by long-lived greenhouse gases: Calculations with the AER radiative transfer models. *J. Geophys. Res.*, **113**, D13103, <https://doi.org/10.1029/2008JD009944>.
- Jiménez, P. A., J. Dudhia, J. F. González-Rouco, J. Navarro, J. P. Montávez, and E. García-Bustamante, 2012: A revised scheme for the WRF surface layer formulation. *Mon. Wea. Rev.*, **140**, 898–918, <https://doi.org/10.1175/MWR-D-11-00056.1>.
- Johnson, A., X. Wang, J. R. Carley, L. J. Wicker, and C. Karstens, 2015: A comparison of multiscale GSI-based EnKF and 3DVar data assimilation using radar and conventional observations for midlatitude convective-scale precipitation forecasts. *Mon. Wea. Rev.*, **143**, 3087–3108, <https://doi.org/10.1175/MWR-D-14-00345.1>.
- Jones, T. A., and Coauthors, 2020: Assimilation of GOES-16 radiances and retrievals into the Warn-on-Forecast System. *Mon. Wea. Rev.*, **148**, 1829–1859, <https://doi.org/10.1175/MWR-D-19-0379.1>.
- Lee, J., E.-H. Lee, and K.-H. Seol, 2019: Validation of integrated multisatellite retrievals for GPM (IMERG) by using gauge-based analysis products of daily precipitation of East Asia. *Theor. Appl. Climatol.*, **137**, 2497–2512, <https://doi.org/10.1007/s00704-018-2749-1>.
- Lin, Y., and K. E. Mitchell, 2005: The NCEP stage II/IV hourly precipitation analyses: Development and applications. Preprints, *19th Conf. on Hydrology*, San Diego, CA, Amer. Meteor. Soc., 1.2, <https://ams.confex.com/ams/pdfpapers/83847.pdf>.

- Lu, X., Y. Wang, and Y. Qiu, 2022: A convection-permitting numerical study of diurnal cycles of pre-summer rainfall over southern China. *Quart. J. Roy. Meteor. Soc.*, **148**, 3677–3693, <https://doi.org/10.1002/qj.4381>.
- Marzban, C., 2004: The ROC curve and the area under it as performance measures. *Wea. Forecasting*, **19**, 1106–1114, <https://doi.org/10.1175/825.1>.
- Mason, P. J., and D. J. Thompson, 1992: Stochastic backscatter in large-eddy simulations of boundary layers. *J. Fluid Mech.*, **242**, 51–78, <https://doi.org/10.1017/S0022112092002271>.
- Minamide, M., and F. Zhang, 2017: Adaptive observation error inflation for assimilating all-sky satellite radiance. *Mon. Wea. Rev.*, **145**, 1063–1081, <https://doi.org/10.1175/MWR-D-16-0257.1>.
- , and —, 2018: Assimilation of all-sky infrared radiances from *Himawari-8* and impacts of moisture and hydrometer initialization on convection-permitting tropical cyclone prediction. *Mon. Wea. Rev.*, **146**, 3241–3258, <https://doi.org/10.1175/MWR-D-17-0367.1>.
- , and —, 2019: An adaptive background error inflation method for assimilating all-sky radiances. *Quart. J. Roy. Meteor. Soc.*, **145**, 805–823, <https://doi.org/10.1002/qj.3466>.
- , and D. J. Posselt, 2021: Hurricane-seasonal analysis on the performances of convection-permitting ensemble tropical cyclone initializations with all-sky satellite radiance assimilation. *25th Conf. on Integrated Observing and Assimilation Systems for the Atmosphere, Oceans, and Land Surface (IOAS-AOLS)*, New Orleans, LA, Amer. Meteor. Soc., 8.4, <https://ams.confex.com/ams/101ANNUAL/meetingapp.cgi/Paper/384263>.
- , F. Zhang, and E. E. Clothiaux, 2020: Nonlinear forecast error growth of rapidly intensifying Hurricane Harvey (2017) examined through convection-permitting ensemble assimilation of *GOES-16* all-sky radiances. *J. Atmos. Sci.*, **77**, 4277–4296, <https://doi.org/10.1175/JAS-D-19-0279.1>.
- Nakanishi, M., and H. Niino, 2004: An improved Mellor–Yamada level-3 model with condensation physics: Its design and verification. *Bound.-Layer Meteor.*, **112**, 1–31, <https://doi.org/10.1023/B:BOUN.0000020164.04146.98>.
- Okamoto, K., Y. Sawada, and M. Kunii, 2019: Comparison of assimilating all-sky and clear-sky infrared radiances from *Himawari-8* in a mesoscale system. *Quart. J. Roy. Meteor. Soc.*, **145**, 745–766, <https://doi.org/10.1002/qj.3463>.
- Otkin, J. A., and R. Potthast, 2019: Assimilation of all-sky SEVIRI infrared brightness temperatures in a regional-scale ensemble data assimilation system. *Mon. Wea. Rev.*, **147**, 4481–4509, <https://doi.org/10.1175/MWR-D-19-0133.1>.
- Ou, T., D. Chen, X. Chen, C. Lin, K. Yang, H.-W. Lai, and F. Zhang, 2020: Simulation of summer precipitation diurnal cycles over the Tibetan Plateau at the gray-zone grid spacing for cumulus parameterization. *Climate Dyn.*, **54**, 3525–3539, <https://doi.org/10.1007/s00382-020-05181-x>.
- Roberts, N. M., and H. W. Lean, 2008: Scale-selective verification of rainfall accumulations from high-resolution forecasts of convective events. *Mon. Wea. Rev.*, **136**, 78–97, <https://doi.org/10.1175/2007MWR2123.1>.
- Ruppert, J. H., Jr., and X. Chen, 2020: Island rainfall enhancement in the Maritime continent. *Geophys. Res. Lett.*, **47**, e2019GL086545, <https://doi.org/10.1029/2019GL086545>.
- Sawada, Y., K. Okamoto, M. Kunii, and T. Miyoshi, 2019: Assimilating every-10-minute *Himawari-8* infrared radiances to improve convective predictability. *J. Geophys. Res. Atmos.*, **124**, 2546–2561, <https://doi.org/10.1029/2018JD029643>.
- Schumacher, R. S., and A. J. Clark, 2014: Evaluation of ensemble configurations for the analysis and prediction of heavy-rain-producing mesoscale convective system. *Mon. Wea. Rev.*, **142**, 4108–4138, <https://doi.org/10.1175/MWR-D-13-00357.1>.
- Schwartz, C. S., 2019: Medium-range convection-allowing ensemble forecasts with a variable-resolution global model. *Mon. Wea. Rev.*, **147**, 2997–3023, <https://doi.org/10.1175/MWR-D-18-0452.1>.
- , and R. A. Sobash, 2017: Generating probabilistic forecasts from convection-allowing ensembles using neighborhood approaches: A review and recommendations. *Mon. Wea. Rev.*, **145**, 3397–3418, <https://doi.org/10.1175/MWR-D-16-0400.1>.
- , G. S. Romine, K. R. Smith, and M. L. Weisman, 2014: Characterizing and optimizing precipitation forecasts from a convection-permitting ensemble initialized by a mesoscale ensemble Kalman filter. *Wea. Forecasting*, **29**, 1295–1318, <https://doi.org/10.1175/WAF-D-13-00145.1>.
- , —, R. A. Sobash, K. R. Fossell, and M. L. Weisman, 2019: NCAR’s real-time convection-allowing ensemble project. *Bull. Amer. Meteor. Soc.*, **100**, 321–343, <https://doi.org/10.1175/BAMS-D-17-0297.1>.
- , —, and D. C. Dowell, 2021: Toward unifying short-term and next-day convection-allowing ensemble forecast systems with a continuously cycling 3-km ensemble Kalman filter over the entire conterminous United States. *Wea. Forecasting*, **36**, 379–405, <https://doi.org/10.1175/WAF-D-20-0110.1>.
- Skamarock, W. C., J. B. Klemp, M. G. Duda, L. D. Fowler, S.-H. Park, and T. D. Ringler, 2012: A multiscale nonhydrostatic atmospheric model using centroidal Voronoi tessellations and C-grid staggering. *Mon. Wea. Rev.*, **140**, 3090–3105, <https://doi.org/10.1175/MWR-D-11-00215.1>.
- , and Coauthors, 2019: A description of the Advanced Research WRF Model version 4. NCAR Tech. Note NCAR/TN-556+STR, 145 pp., <https://doi.org/10.5065/1dfh-6p97>.
- Surcel, M., I. Zawadzki, and M. K. Yau, 2015: A study on the scale dependence of the predictability of precipitation patterns. *J. Atmos. Sci.*, **72**, 216–235, <https://doi.org/10.1175/JAS-D-14-0071.1>.
- Takaya, Y., I. Ishikawa, C. Kobayashi, H. Endo, and T. Ose, 2020: Enhanced Meiyu-Baiu rainfall in early summer 2020: Aftermath of the 2019 super IOD event. *Geophys. Res. Lett.*, **47**, e2020GL090671, <https://doi.org/10.1029/2020GL090671>.
- Tewari, M., and Coauthors, 2004: Implementation and verification of the unified Noah land surface model in the WRF model. *20th Conf. on Weather Analysis and Forecasting/16th Conf. on Numerical Weather Prediction*, Seattle, WA, Amer. Meteor. Soc., 14.2a, https://ams.confex.com/ams/84Annual/techprogram/paper_69061.htm.
- Thompson, G., and T. Eidhammer, 2014: A study of aerosol impacts on clouds and precipitation development in a large winter cyclone. *J. Atmos. Sci.*, **71**, 3636–3658, <https://doi.org/10.1175/JAS-D-13-0305.1>.
- , P. R. Field, R. M. Rasmussen, and W. D. Hall, 2008: Explicit forecasts of winter precipitation using an improved bulk microphysics scheme. Part II: Implementation of a new snow parameterization. *Mon. Wea. Rev.*, **136**, 5095–5115, <https://doi.org/10.1175/2008MWR2387.1>.
- Wang, S., A. H. Sobel, F. Zhang, Y. Q. Sun, Y. Yue, and L. Zhou, 2015: Regional simulation of the October and November MJO events observed during the CINDY/DYNAMO field campaign at gray zone resolution. *J. Climate*, **28**, 2097–2119, <https://doi.org/10.1175/JCLI-D-14-00294.1>.
- Weng, Y., and F. Zhang, 2012: Assimilating airborne Doppler radar observations with an ensemble Kalman filter for convection-permitting hurricane initialization and prediction: Katrina

- (2005). *Mon. Wea. Rev.*, **140**, 841–859, <https://doi.org/10.1175/2011MWR3602.1>.
- Wilks, D. S., 2011: *Statistical Methods in the Atmospheric Sciences*. 3rd ed. International Geophysics Series, Vol. 100, Academic Press, 704 pp.
- Xiao, Q., and J. Sun, 2007: Multiple-radar data assimilation and short-range quantitative precipitation forecasting of a squall line observed during IHOP_2002. *Mon. Wea. Rev.*, **135**, 3381–3404, <https://doi.org/10.1175/MWR3471.1>.
- Xu, W., and E. J. Zipser, 2011: Diurnal variations of precipitation, deep convection, and lightning over and east of the eastern Tibetan Plateau. *J. Climate*, **24**, 448–465, <https://doi.org/10.1175/2010JCLI3719.1>.
- Yussouf, N., J. S. Kain, and A. J. Clark, 2016: Short-term probabilistic forecasts of the 31 May 2013 Oklahoma tornado and flash flood event using a continuous-update-cycle storm-scale ensemble system. *Wea. Forecasting*, **31**, 957–983, <https://doi.org/10.1175/WAF-D-15-0160.1>.
- Zhang, F., C. Snyder, and J. Sun, 2004: Impacts of initial estimate and observation availability on convective-scale data assimilation with an ensemble Kalman filter. *Mon. Wea. Rev.*, **132**, 1238–1253, [https://doi.org/10.1175/1520-0493\(2004\)132<1238:IOIEAO>2.0.CO;2](https://doi.org/10.1175/1520-0493(2004)132<1238:IOIEAO>2.0.CO;2).
- , Y. Weng, J. A. Sippel, Z. Meng, and C. H. Bishop, 2009: Cloud-resolving hurricane initialization and prediction through assimilation of Doppler radar observations with an ensemble Kalman filter. *Mon. Wea. Rev.*, **137**, 2105–2125, <https://doi.org/10.1175/2009MWR2645.1>.
- , M. Minamide, and E. E. Clothiaux, 2016: Potential impacts of assimilating all-sky infrared satellite radiance from GOES-R on convection-permitting analysis and prediction of tropical cyclones. *Geophys. Res. Lett.*, **43**, 2954–2963, <https://doi.org/10.1002/2016GL068468>.
- , —, R. G. Nystrom, X. Chen, S.-J. Lin, and L. M. Harris, 2019: Improving Harvey forecasts with next-generation weather satellites: Advanced hurricane analysis and prediction with assimilation of GOES-R all-sky radiances. *Bull. Amer. Meteor. Soc.*, **100**, 1217–1222, <https://doi.org/10.1175/BAMS-D-18-0149.1>.
- Zhang, Y., F. Zhang, D. J. Stensrud, and Z. Meng, 2016: Intrinsic predictability of the 20 May 2013 tornadic thunderstorm event in Oklahoma at storm scales. *Mon. Wea. Rev.*, **144**, 1273–1298, <https://doi.org/10.1175/MWR-D-15-0105.1>.
- , —, and —, 2018: Assimilating all-sky infrared radiances from GOES-16 ABI using an ensemble Kalman filter for convection-allowing severe thunderstorms prediction. *Mon. Wea. Rev.*, **146**, 3363–3381, <https://doi.org/10.1175/MWR-D-18-0062.1>.
- , D. J. Stensrud, and F. Zhang, 2019: Simultaneous assimilation of radar and all-sky satellite infrared radiance observations for convection-allowing ensemble analysis and prediction of severe thunderstorms. *Mon. Wea. Rev.*, **147**, 4389–4409, <https://doi.org/10.1175/MWR-D-19-0163.1>.
- , —, and E. E. Clothiaux, 2021a: Benefits of the Advanced Baseline Imager (ABI) for ensemble-based analysis and prediction of severe thunderstorms. *Mon. Wea. Rev.*, **149**, 313–332, <https://doi.org/10.1175/MWR-D-20-0254.1>.
- , X. Chen, and Y. Lu, 2021b: Structure and dynamics of ensemble correlations for satellite all-sky observations in an FV3-based global-to-regional nested convection-permitting ensemble forecast of Hurricane Harvey. *Mon. Wea. Rev.*, **149**, 2409–2430, <https://doi.org/10.1175/MWR-D-20-0369.1>.
- , E. E. Clothiaux, and D. J. Stensrud, 2022a: Correlation structures between satellite all-sky infrared brightness temperatures and the atmospheric states at storm scales. *Adv. Atmos. Sci.*, **39**, 714–732, <https://doi.org/10.1007/s00376-021-0352-3>.
- , H. Yu, M. Zhang, Y. Yang, and Z. Meng, 2022b: Uncertainties and error growth in forecasting the record-breaking rainfall in Zhengzhou, Henan on 19–20 July 2021. *Sci. China Earth Sci.*, **65**, 1903–1920, <https://doi.org/10.1007/s11430-022-9991-4>.
- Zhao, J., J. Gao, T. A. Jones, and J. Hu, 2021: Impact of assimilating high-resolution atmospheric motion vectors on convective scale short-term forecasts: 2. Assimilation experiments of GOES-16 satellite derived winds. *J. Adv. Model. Earth Syst.*, **13**, e2021MW002486, <https://doi.org/10.1029/2021MS002486>.